Department of Physics and Astronomy
University of Heidelberg

Master's Thesis in Physics
submitted by

Jan Hendrik Willibald Becher

born in Limburg an der Lahn

2016

Towards Spin and Site-Resolved, Single-Atom Imaging of ^{6}Li Atoms in a Multiwell Potential

This Master Thesis has been carried out by Jan Hendrik Willibald Becher at the
Physikalisches Institut Heidelberg
under the supervision of
Prof. Selim Jochim

Abstract

This master's thesis reports on the realization and characterization of a single-atom imaging setup for fermionic ^{6}Li atoms via fluorescence imaging. It will have the potential of resolving both the spin and the site of the atom in our multi-well potential. In our experiment we can deterministically prepare single atoms in a tightly focused optical potential. We can initialize the atom in one of the three lowest hyperfine states of the ground state of ^{6}Li. For imaging an atom in either state, we illuminate the atom with two counterpropagating laser beams, resonant to the D_2 transition and collect the scattered photons with a high-resolution objective onto an EMCCD-camera. Within an imaging time of $11\,\mu$s, we detect around 15 photons on the camera with single-photon resolution. This enables us to detect a single atom with a fidelity of around $(96 \pm 5)\,\%$.
We image the atoms in high magnetic fields, where the three lowest hyperfine states of the ground-state of ^{6}Li are separated by around 80 MHz. At values above 900 G, there is a closed optical transition for each spin state such that we can address each spin state individually. This will allow us to perform spin resolved imaging.
Furthermore we plan to have site-resolution by separating the individual wells further than the diffusion of the atom during the imaging process.

Zusammenfassung

Diese Masterarbeit beschreibt und charakterisiert einen neuen Aufbau, der es uns ermöglicht, einzelne ^{6}Li Atome mit einer Fluoreszenzabbildung abzubilden. Unsere Herangehensweise hat das Potential, spin- und ortsaufgelöste Bilder von einzelnen Atomen in einem kleinen optischen Gitter zu machen.
In unserem Experiment können wir ein einzelnes Atome auf deterministische Art in einem stark fokussierten optischen Potential präparieren. Dieses Atom kann in jedem der drei niedrigsten Hyperfein-Level des Grundzustands von ^{6}Li initialisiert werden. Um ein einzelnes Atom in einem dieser drei Zustände abzubilden, belichten wir das Atom mit zwei zur D_2 Linie resonanten, gegenläufigen Laserstrahlen und fokussieren die gestreuten Photonen mit einem hochauflösendem Objektiv auf eine EMCCD-Kamera. Innerhalb von $11\,\mu$s detektieren wir im ungefähr 15 Photonen auf der Kamera mit einer Auflösung von einzelnen Photonen. Dies ermöglicht uns, einzelne Atome mit einer Wahrscheinlichkeit von $(96 \pm 5)\,\%$ zu identifizieren.
In starken magnetischen Feldern sind die drei niedrigsten Hyperfeinzustände des Grundzustandes von ^{6}Li um etwa 80 MHz getrennt. Bei Feldern über 900 G besitzt jeder der drei Zustände einen geschlossenen optischen Übergang, sodass wir jeden Spinzustand einzeln adressieren können. Dies wird und ermöglichen, spinaufgelöste Bilder zu nehmen.
Außerdem planen wir, die Atome örtlich aufzulösen, indem wir die einzelnen Potentialtöpfe weiter auseinanderfahren, als das Atom diffundiert, während wir es belichten.

Contents

1 Introduction

Many interesting macroscopic physical effects or phases stem from the complex behavior of a many-body quantum state. In some cases such phases can be well described by mean-field approaches such as the famous BCS-theory for conventional superconductivity or the description of the ground state of a weakly interacting Bose gas. However, especially for strongly interacting and correlated systems, effective theories fail and cannot reveal the mechanisms that are responsible for curious behavior of a many-body state. For states with long-ranged correlations the complexity of an accurate description increases exponentially with system size, which makes it literally impossible to simulate such systems on a classical computer. Already the numerical simulation of a system of 50 atoms is far out of reach with classical computers [1].

In order to circumvent this problem, Feynman introduced the concept of Quantum Simulation [2]. His idea was to experimentally explore quantum mechanical systems in the laboratory, whose behavior is governed by the same Hamiltonian as the system of interest. For example instead of studying electrons in a solid one could use an ultracold gas of fermionic neutral atoms, trapped in an almost perfect periodic potential. Due to the much larger size and the longer time scales, such a system is much easier to investigate experimentally.

In order to realize such systems in the laboratory, several criteria have to be fulfilled [3]. We need a quantum system of bosons or fermions with many degrees of freedom with a good control over the motional states. It is necessary that the system can be initialized into a well known quantum state. Once the system has been initialized, we need to engineer interactions of a particle with both external fields and other particles and have access to Hamiltonians that cannot be simulated on classical computers. After a quantum simulation, it is necessary to probe the final state with a method that allows the reconstruction of an observable of interest. An effective readout also requires a reliable initialization in order to perform the same measurement several times. The last criterion of a quantum simulator is the possibility to probe the outcome of the quantum simulation by simulating systems to which a solution is known.

For using ultracold quantum gases as a quantum simulator, a gas of atoms must be cooled to very low temperatures such that the de-Broglie wavelength of the particles becomes comparable to the interparticle spacing. At such ultra low temperatures, neutral atoms can be trapped in optical potentials [4] which can be shaped to almost arbitrary forms [5, 6, 7]. Furthermore such quantum gases feature a high controllability over the internal degrees of freedom which can be exploited for the engineering of complex Hamiltonians [8, 9]. This high controllability allows to initialize and manipulate the quantum state of the system with very high precision even on the single-atom level [10]. Using a magnetic field it is possible to tune the s-wave scattering length via Feshbach resonances and thereby engineer a tunable interaction between the particles. Also other atomic properties such as large magnetic moments [11], higher order Feshbach resonances [12], processes such as the superexchange [13, 14] or artificial magnetic fields [15] can be employed to model longer ranged interactions or to simulate the coupling to gauge fields and thus to initialize systems with more complex Hamiltonians in the laboratory.

Not only the initialization and manipulation of ultracold atoms has made huge progress, also the read out of the quantum state made advances. Depending on the observable that needs to be measured, different methods are applied. The momentum distribution of the atomic sample can be accessed in time-of-flight imaging [16, 17]. Analysis of noise correlations in the atomic density [18] can reveal correlations between the particles in the atomic sample. Recently, with the realization of quantum gas microscopes for both bosonic [1, 19] and fermionic atoms [20, 21, 22, 23] it became possible to probe the many-body in-situ density distribution at the single-atom level. Single-site resolution enables to probe the formation of different phases in an optical lattice on a single-atom level as for example the phase transition from a Mott insulator to a superfluid [24].

Each readout method has its own advantages but the reconstruction of the whole quantum state is still a challenging problem. A big issue in most systems is the resolution of the spin state of the individual atoms which is very cumbersome to achieve [25]. Furthermore, light assisted collisions when more than one particle is occupying the same site of a lattice restricts many quantum gas microscopes to measuring only the parity of the atom number on each site which can only be avoided with a huge experimental effort [25, 26].

In our experiment, we can deterministically prepare two fermions in the ground state of an isolated double-well potential [27]. Such a system realizes the fundamental building block of the Hubbard model. With our approach we can control each site

of the potential separately and we have the full control over the quantum state of the system. This enables us to repeatedly initialize the system in its ground state with very high fidelity.
We are able to add more wells to the double-well potential and to expand the system to an array of lattice sites with the full control over each site. For future experiments we want to have a fast imaging system that gives us access to the spin-resolved in-situ density distribution with single-atom resolution in the multi-well potential. With this we realize a quantum simulator for few atoms which can be expanded towards a larger system.

Outline

In this thesis I will report on the implementation of a single atom imaging setup with the potential of resolving both the spin state and the site-resolved location in a multi-well potential. The next chapter gives an overview on this imaging setup and its challenges and estimates the most important parameters. Our experimental apparatus and the deterministic preparation scheme for few atoms is briefly described in Chapter 3. For spin resolved imaging, it is necessary to carefully analyze the imaging transitions in ^{6}Li as will be done in detail in Chapter 4. For the detection of single photons during the imaging process, we employ an EMCCD camera. The working principle of the camera is described and the camera is characterized in Chapter 5. The last chapter will present the first results of the imaging system and different methods to identify single atoms, before I give a summary and an outlook on the next steps to complete the imaging procedure.

2 Single Atom, Site-Resolved Imaging in Lattice Systems

In a recent experiment, we realized the fundamental building block of the Fermi-Hubbard model by preparing two ^{6}Li atoms in the ground state of an isolated double-well potential [27]. This potential was realized with two partly overlapping tightly focused optical dipole traps. By adding more of these dipole traps, we can expand our system to an array of optical tweezers, forming a small optical lattice, in which we want to deterministically prepare few atoms in the many-body ground state. This idea is illustrated in Figure 2.1.

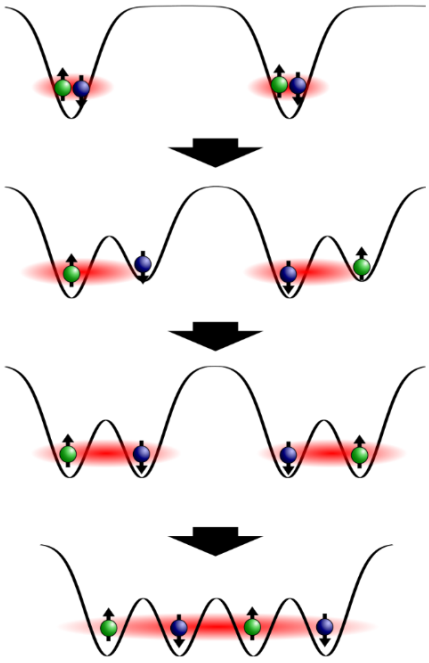

Figure 2.1: In our experiment we can deterministically prepare few atoms in single trapping potentials. By merging these systems, we want to expand the system in order to approach the many-body limit with a bottom-up approach.

In order to read out the quantum state at the end of the experimental sequence, we

so far used an imaging technique that allowed us to count the total number of atoms with very high fidelity. For this we switch off the trapping potential and recapture the atoms that are still present in a magneto-optical trap. Then we collect the fluorescence signal of the atoms. Figure 2.2 shows example images of this detection technique. Although one can count atom numbers up to 1000 on a single atom level with this technique [28], we lose information about the position and the spin of the individual atoms. In order to reconstruct the full quantum state, we have to perform complicated experimental schemes before the detection which become harder and time consuming for larger systems. For future experiments, we thus aim for an in-situ imaging with site and spin-resolution.

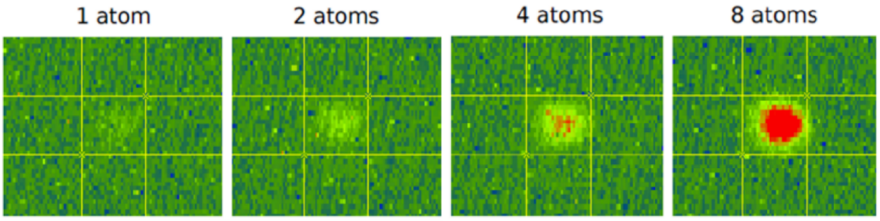

Figure 2.2: To detect the number of atoms, we switch off the trapping potential and recapture the atoms into a magneto-optical trap. With this method we can count up to around 20 atoms with very high fidelity.

2.1 The common approach: Quantum Gas Microscopes

The common approach for site-resolved imaging of optical lattice systems is a quantum gas microscope which has recently been realized for both bosonic [19, 1] and fermionic [20, 21, 22, 23] atoms. These microscopes probe the atom-resolved in-situ density distribution of the system via fluorescence imaging. This allows for example to directly observe the quantum phase transition from a Mott-insulator to a superfluid [24, 29]. In order to achieve the site-resolution, two requirements have to be fulfilled.

First a high resolution imaging system is needed that is able to resolve the lattice spacing. Typical lattice spacings in optical lattices are on the order of 500-750 nm. To resolve the individual sites of the lattice, a higher resolution is required. Our high-resolution objective with a numerical aperture of $NA \approx 0.55$ can achieve a diffraction-limited resolution of $d = 0.61\frac{\lambda}{NA} \approx 750\,\mathrm{nm}$ when imaging on the D_2 line

of ^{6}Li with 671 nm. A shorter transition wavelength and higher numerical apertures can achieve even higher resolutions. Furthermore, images can be post processed to further increase the resolution by exploiting the periodic lattice potential [29].
The second demand requires much more effort and is harder to realize. To access the in-situ density distribution of the atoms, diffusion and hopping of the atoms to neighboring lattice sites must be prohibited during the imaging process.
In conventional quantum gas microscopes, the particle distribution in the lattice is frozen by ramping the lattice deep in order to enter the Lamb-Dicke regime. In this regime the photon recoil energy E_{rec} is much smaller than the quantized energy spacing $\hbar\omega_{trap}$ of the harmonic trap and therefore inelastic scattering is suppressed. This regime is characterized by the Lamb-Dicke parameter $\eta = \sqrt{\frac{E_{rec}}{\hbar\omega_{trap}}}$. In order to fulfill $\eta \ll 1$, very strong lattice beams with several watts laser power are required. Despite the suppression of inelastic scattering events in this regime, the average increase in energy per scattered photons is twice the recoil energy [30]. Hence during the imaging process the atomic sample heats up. The atoms only need to scatter few photons to gain enough energy to start hopping to neighboring sites, and so additional mechanisms such as Sisyphus or Raman-sideband cooling have to be applied to keep the atoms localized on their lattice site.
This enables to image the atoms in the lattice over around one second to collect a few thousand photons per atom [29]. One drawback of this method is that by entering the Lamb-Dicke regime, the atomic density on each site becomes so large, that atom pairs are immediately lost due to light assisted collisions. Therefore most quantum gas microscopes can only detect the particle number modulo two. Furthermore, one issue of quantum gas microscopes is spin-resolved imaging. Both number and spin-resolved imaging have been demonstrated in optical lattices but it is cumbersome to achieve [25, 26].

2.2 An alternative approach

For the identification of a single atom with a high fidelity, one needs to detect a signal above the noise level of the imaging setup. Conventional quantum gas microscopes do this by keeping the atoms pinned to their lattice site to collect thousands of photons. However, with the appropriate equipment, one can detect very low photon numbers with single photon resolution. By using an EMCCD camera (Electron Multiplying CCD), already an average number of 20 detected photons produces a signal above the noise level of the camera. This makes both pinning of the atoms in a deep potential and additional cooling mechanisms unnecessary. To achieve site

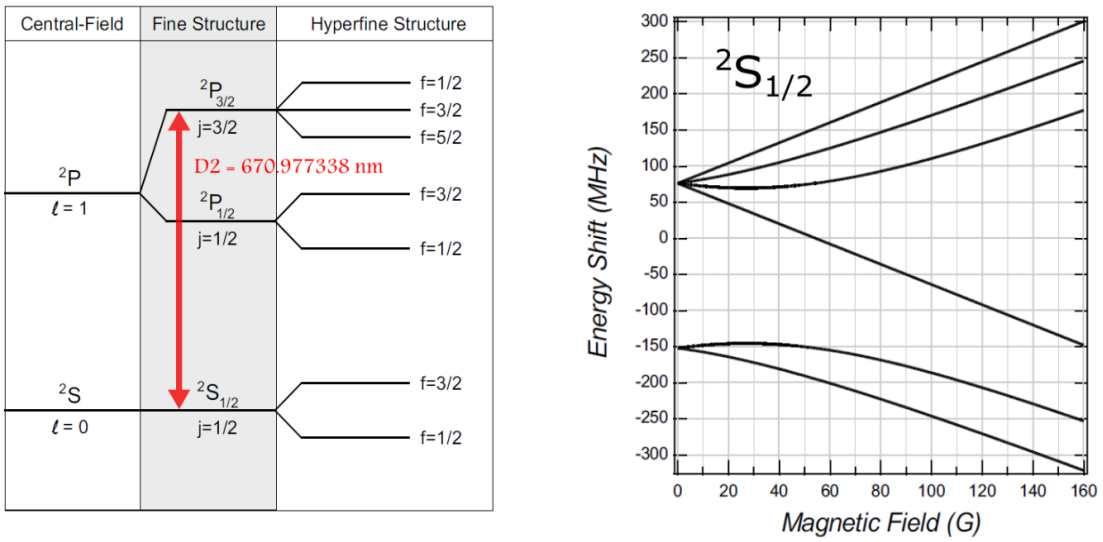

Figure 2.3: The left image shows the level structure of the lowest levels in ^{6}Li . We image the atoms on the D_2 line. The right graph shows the dependence of the ground state energies on the magnetic field. Due to the large hyperfine splitting of the ground state, we can address the different hyperfine states separately. With this we can resolve the spin distribution in the multiwell potential. Figure taken and adapted from [31].

resolution, one can either try to counter the diffusion of the atoms by trying to keep the atoms trapped in their potential or, as we can do with our approach, increase the spacing between the individual sites to a distance that is much larger than the diffusion length before imaging the system.

Our imaging scheme for single-atom, site-resolved imaging

With a numerical aperture of $NA \approx 0.55$, our high-resolution objective collects around 11.4% of the scattered photons. Here we profit from the dipole radiation pattern as is explained in 4.3. The collected fluorescence light is focused onto the EMCCD camera, which has a quantum efficiency of around 85 %. The setup is illustrated in Figure 2.4. We image on the D_2-line of ^{6}Li with a wavelength of $\lambda = 670.977338\,\text{nm}$ and a natural linewidth of $\Gamma = 5.8724\,\text{MHz} = 36.898 \times 10^6\,\text{s}^{-1}$ [31]. This corresponds to a lifetime in the excited state of $\tau = 27.1\,\text{ns}$ and a maximal scattering rate of $\gamma_{max} = \Gamma/2 = 18.45\,\text{photons}/\mu\text{s}$. In order to collect 20 photons per atom with these parameters we need an imaging time of at least $11\,\mu\text{s}$. One drawback of ^{6}Li as the lightest alkali atom is the high atomic recoil velocity of $v_{rec} = 9.887\,\text{cm/s}$ and the recoil temperature of $T_{rec} = 3.54\,\mu\text{K}$ which causes a fast diffusion. Assuming a 3D random walk in momentum space for the absorption and

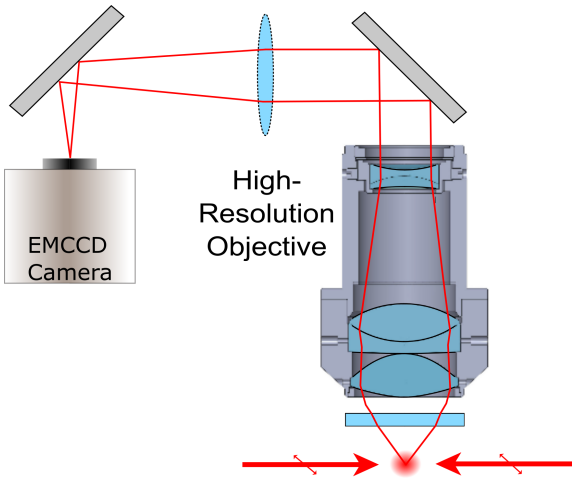

Figure 2.4: We illuminate the atoms with two counterpropagating, horizontally polarized laser beams, resonant to the D_2 transition. We collect around 11.4 % of the scattered photons with a high-resolution objective and focus the signal onto an EMCCD. Within an imaging time of 11 μs, we detect around 20 photons on the camera with single-photon resolution.

spontaneous emission during the imaging process, this number of scattering events corresponds to a velocity spread of $\sigma_v \approx 0.56\,\mu\text{m}/\mu\text{s}$ which causes a diffusion on the order of $\sigma_x \approx 3\,\mu$m as will be analyzed in Section 4.6. Hence by separating two wells to a distance of 10 μm we can achieve site resolution.
Ti improve the resolution of the imaging system, the diffusion can be countered by increasing the power of the trapping beam. For this we ramp the laser power to around 10 mW. With a beam waist of 1.3 μm this corresponds to around $42E_{rec}$ in the ground state and $28E_{rec}$ in the excited state [32]. This helps to better localize the atoms such that the signal is distributed over less pixels.

Towards spin resolved imaging

We image the atoms at magnetic fields of around 900 G. We do this for two reasons. On the one hand, if we do not want to add a repumper to our system, we need a closed optical transition which we only have at such magnetic fields. The other reason is that it enables to address the different spin states individually. As shown in Figure 2.3, the different sublevels of the ground state split up with increasing magnetic field. The splitting between the three lowest states at typical fields is on the order of 80 MHz which is much larger than the linewidth of both the imaging laser and the D_2-line. This splitting enables us to image the different spins individually. For the spin-resolved imaging, we will use our camera in fast kinetics mode which allows us to take two images with a delay of only some microseconds. To probe the

spin resolved density-distribution, we image each spin state separately. For this we tune the laser frequency resonant to the first spin state for the first image and then jump with the laser frequency to become resonant with the other spin state for the second image.
This approach also has a huge advantage when more than one atom is occupying the same well. Due to the low atomic density during the imaging process, losses caused by light assisted collisions can be neglected and counting of atoms in the same well becomes possible. As will be discussed in 6.2, we need to detect around 40 photons per atom on average in order to clearly separate the signal of one and two identical atoms. With some improvements to our system, this might soon be achievable. However, if two different spin states are sitting on the same site, taking one image per spin states only requires around 10 photons per atom. Thus it becomes very easy to identify two distinguishable atoms on the same site.

With our approach, there is no need for powerful lasers or for complex cooling mechanisms. Moreover we are able to image at high magnetic fields which will give us access to the spin-resolved density distribution. However this requires a good understanding of both the imaging transitions and the working principle of the EMCCD camera. For completeness, the next chapter briefly explains our experimental setup and how we initialize our system. The relevant chapters for the imaging of single atoms are Chapter 4, [**?**] and 6.

3 Experimental Setup

The deterministic preparation and the coherent manipulation of a ground-state system of few fermions requires many different experimental steps. This chapter will summarize our experimental sequence to prepare single atoms. We start from a hot sample of ^{6}Li-atoms, cool them down into the quantum degenerate regime and then transfer atoms into an array of tightly focused optical dipole traps in which we deterministically prepare few atoms.

3.1 Vacuum chamber and Zeeman slower

For a stable experiment, the atomic sample must be isolated from the environment. Hence we need an ultra-high vacuum on the order of 10^{-12} mbar inside the experiment chamber to avoid any collisions with background gases. Figure 3.1 shows the basic setup of our vacuum chamber. The vacuum is produced by two titanium sublimator pumps (1) and two ion pumps (2). In order to prevent outgasing of the underlying substrate, the walls of the science chamber (5) are coated with a non-evaporable getter coating. Furthermore, this coating can be used to pump residual atoms once it gets activated at 180 °C.
The first step of the experiment is the production of a beam of ^{6}Li -atoms. For this, lithium is heated up in the oven chamber (3) to around 360 °C and then emitted through a conical tube under an emission angle of $\alpha \approx 12°$. There are two gate valves (6) which can be used to seal off parts of the experiment so that for example the oven can be refilled without breaking the vacuum in the science chamber. An atomic beam shutter has been implemented between the oven chamber and the first gate valve to interrupt the beam of ^{6}Li -atoms after the first step of the experiment which is the loading of the Magneto-Optical Trap (MOT).
A counterpropagating laser beam, resonant to the D2 transition, is used to slow down the hot atomic beam on their way to the science chamber. Due to the decreasing velocity in the slowing process, the resonance frequency is doppler shifted which is compensated with a decreasing magnetic field generated by the Zeeman slower coils (4). The Zeeman slower consists of eight coils with different winding numbers so

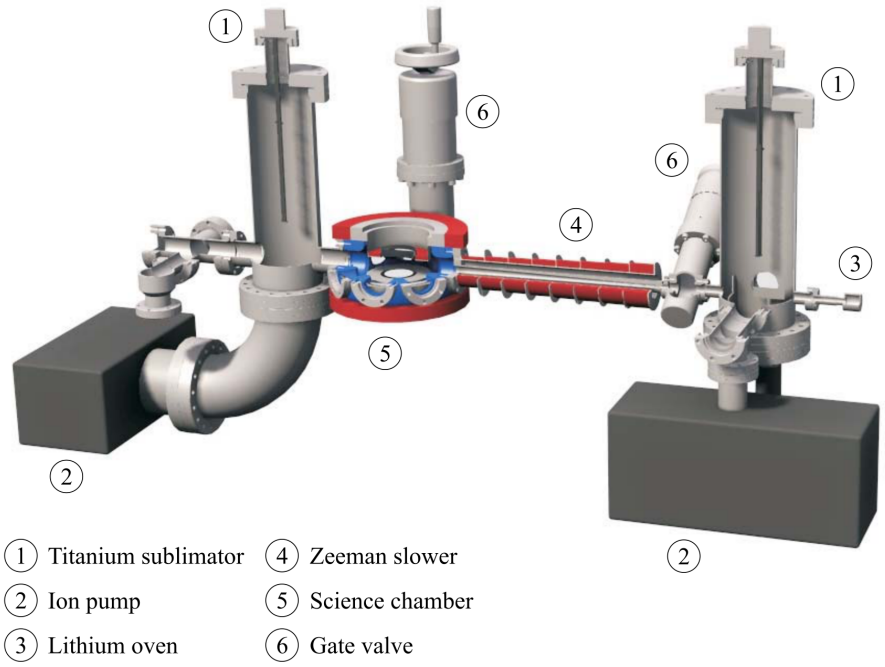

Figure 3.1: The figure illustrates the vacuum chamber of the experiment. For our experiments, we need an ultra high vacuum of $P \approx 10^{-11}$ mbar. Atoms get heated in the oven and slowed down with a Zeeman-slower. A MOT captures the atoms in the science chamber where the actuel axperiment is performed. In total 8 windows give good optical access to the atoms. Figure taken from [33]

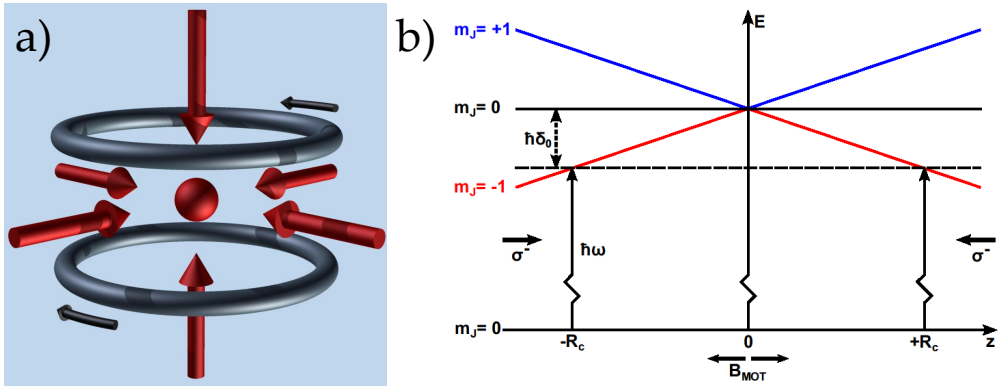

Figure 3.2: The left picture shows the configuration of a Magneto-Optical Trap. Six counterpropagating laser beams from all three spatial dimensions create a so called optical molasses. In order to prevent particles from diffusing out of the molasses, two coils in an anti-Helmholz configuration create a constant magnetic field gradient. By choosing σ_--polarized light, atoms become resonant due to the Zeeman-effect as is shown in the right graph.

that the magnetic field decreases when the atoms approach the science chamber. The light pressure of the resonant laser beam slows down the atoms from an initial velocity of around 800 m/s to a final velocity of 60 m/s which is slow enough to be captured by the MOT. A more detailed characterization of the Zeeman slower can be found in [34].

3.2 Trapping and cooling ^{6}Li -atoms

In order to achieve very low temperatures and entropies, we need to cool down the atoms into the quantum degenerate regime. For this purpose, the atoms are cooled and prepared in a three step process. The first step is to capture the atoms in a MOT where they are cooled to a temperature of $T = 200\,\mu$K. The atoms are then transfered into a crossed beam dipole trap where the atoms are evaporatively cooled to a temperature of 250 nK. By applying a tightly focused red-detuned laser beam to this sample, we use a spilling scheme that allows us to deterministically prepare few atoms in the ground-state of a quasi one-dimensional trap.

3.2.1 Trapping and cooling in a magneto-optical trap (MOT)

A Magneto optical trap relies on the interplay between the light force of counter-propagating laser beams and the linear Zeeman-shift, introduced by a magnetic field gradient. The working principle is illustrated in Figure 3.2. In order to capture atoms inside a MOT, two counterpropagating, red-detuned laser beams are applied

in each of the three spatial dimensions. Due to the absorption of photons, atoms inside the MOT experience a light force from each of the six laser beams. If the atom is resting, the light forces from opposite laser beams cancel and the atom does not get accelerated. If the atom is moving along one axis, it becomes more resonant to its counterpropagating laser beam due to the the Doppler effect. This increases the probability to absorb a photon with the opposite momentum such that the light force decelerates the atom. However this restoring force vanishes when the atom is resting again and is not able to bring it back to the trap center. It only introduces strong damping of the atomic velocity (that is why this state is called an optical molasses). With this configuration, atoms are slowed down but not trapped since slow atoms may diffuse out of the optical molasses without getting resonant to a laser beam. In order to prevent this diffusion, a constant magnetic field gradient is added via two coils in an anti-Helmholtz configuration. Atoms, that are slowly diffusing out of the optical molasses, experience an increasing magnetic field, that, due to the Zeeman-effect, shifts the resonance frequency such that they become resonant to the counterpropagating red-detuned laser beam. For this the polarization of the laser beams have to match the resonant transition. As shown in Figure 3.2(b) for a simplified 1D-system, the laser beams require a σ_- polarization such that a red-detuned laser beam gets resonant to the $m_J = -1$ state. Overall this configuration has both a velocity and a position dependent restoring force which allows to trap neutral atoms.

In our experiment we use three retro reflected laser beams that are red-detuned to the D_2-transition of ^{6}Li by approximately $6\,\Gamma$, with $\Gamma = 2\pi \times 5.8724\,\mathrm{MHz}$ being the natural line width of the D_2-transition. As was already shown in Figure 2.3, the hyperfine splitting of the $2^2P_{3/2}$ state at vanishing magnetic field is 4.4 MHz and can therefore not be resolved since it is smaller than the natural linewidth of around 6 MHz. Atoms in the excited state can decay into both hyperfine levels of the ground state, which are separated by 228 MHz. Hence atoms can get non-resonant if they decay into the (wrong) hyperfine level of the ground state. Due to the decay into the non-resonant states, we need an additional repumping laser, that excites the atoms from the $F = 1/2$ manifold back to the exited state.

The temperature of a MOT is intrinsically limited by the process of absorption and spontaneous emission of photons. For ^{6}Li atoms, this so called Doppler temperature is

$$T_D = \frac{\hbar\Gamma}{2k_B} = 141\,\mu\mathrm{K}. \tag{3.1}$$

Hence we need a second cooling step to achieve low enough temperatures.

3.2.2 Evaporative cooling in an optical dipole trap

The temperature of the atoms in the MOT is still too high for the deterministic preparation of few-atom systems. The next step in the cooling process is evaporative cooling in an optical dipole trap. The idea of evaporative cooling is to trap the atoms in a conservative potential and remove fast atoms from the trap while allowing the remaining ones to rethermalize. By incrementally decreasing the depth of the potential, fast atoms can be removed from the trap. Hence the energy and the temperature in the system are constantly decreased. Due to the fermionic nature of ^{6}Li , the scattering crossection for identical atoms decreases rapidly with temperature. The reason for this is that cold ^{6}Li-atoms only interact via the s-wave contact interaction but identical fermions have zero probability to be at the same spot. Since a rapid thermalisation of the atomic sample is essential for an effective cooling process, we need a balanced mixture of at least two different spin sates in the dipole trap. For this we choose the two lowest hyperfine states of ^{6}Li .

For the creation of a conservative potential, one makes use of the dipole force, which relies on the interaction of an induced dipole moment $\vec{p}$ with the oscillating electric field $\vec{E}$ of a laser beam.

$$\vec{p} = \alpha \vec{E} \tag{3.2}$$

with α being the polarizibility of the atom. For a two level atom, the dipole moment experiences a dipole potential of the from [4]

$$U_{dip}(r) = -\frac{1}{2\epsilon_0 c} Re(\alpha) I(r) = -\frac{3\pi^2}{2\omega_0^3} \Gamma \Big((\omega_0 - \omega)^{-1} + (\omega_0 + \omega)^{-1} \Big) I(r) \tag{3.3}$$

with ω_0 being the resonance frequency of the optical transition, ω the frequency of the electric field, i.e. of the laser beam. Γ is the linewidth of the resonance and $I(r)$ the intensity of the laser beam. A red-detuned laser therefore creates an attractive potential whereas a blue-detuned laser can be used for repulsive potentials. The trapping potential is directly proportional to the intensity of the laser beam so that also more complex trapping geometries can be created by shaping the laser beam. Hence a gaussian beam creates a gaussian potential in radial direction and a Lorenzian potential in axial direction.

For our dipole traps we use a far red-detuned, focused laser beam with a wavelength of 1064 nm and a maximum power of 200 W. The light is taken from a Ytterbium doped-fiber laser (YLR-200-LP) from IPG Photonics. The beam is focused onto the atomic sample trapped in the MOT and reflected to obtain a crossed beam dipole trap with an intersection angle of 14 °. We need such high laser powers to make the

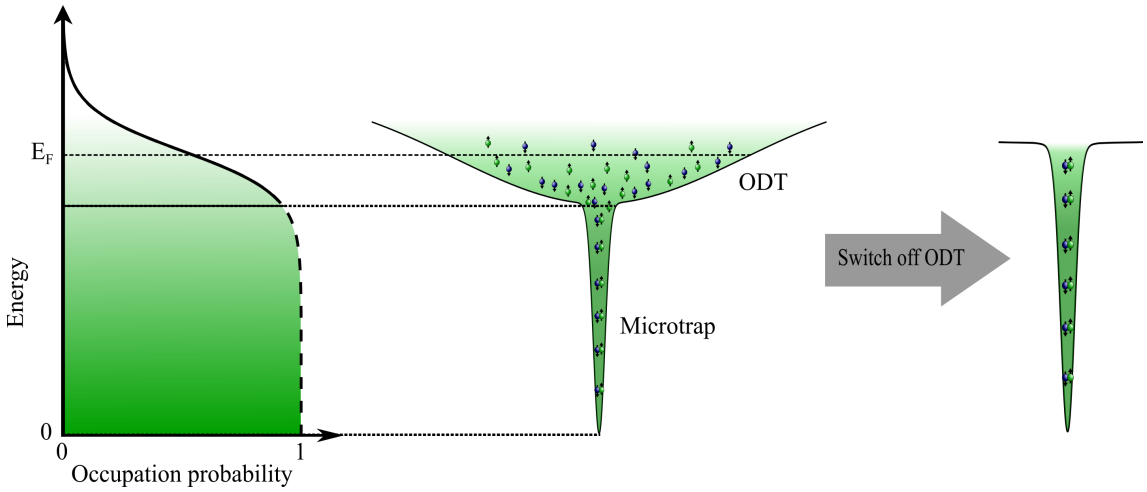

Figure 3.3: The microtrap is created by focusing a 1064 nm beam with our high-resolution objective to a beam waist of 1.3 μm. The tightly focused beam creates a dimple in the large dipole trap. Due to the relatively high Fermi energy and the low temperature, the occupation probability of the lowest level is almost 1. We switch off the large optical dipole trap (ODT) to retain a highly degenerate fermionic gas.

transfer into the dipole trap efficient.

As explained above, by slowly decreasing the overall power in the laser beam, the potential gets more shallow so that atoms with relatively high energy can escape from the trap. With this technique we can prepare around 40.000 atoms at a temperature of $T/T_{Fermi} = 0.5$. This is sufficiently low temperatures to deterministically prepare few atoms as is explained in the next section.

3.3 Deterministic preparation and detection of single atoms

Cooling the atoms as described above is the common approach for the preparation of a sample of ultracold atoms. From here we can prepare few atoms in the ground state of potential with high fidelity by adding a tightly focused dipole trap via a high-resolution objective.

3.3.1 The Dimple-Trap and the Spilling-Scheme

Once we have reached sufficiently low temperatures in the optical dipole trap, we shine in a second 1064 nm laser beam through our high-resolution objective, perpendicular to the crossed beam dipole trap. This is the same objective that we use for

the new imaging setup. It produces a beam waist of 1.3 μm in the focal plane. By overlapping this beam with the large dipole trap, a potential as shown in Figure 3.3 is realized. Due to its shape, this trap is called dimple trap. In order to not heat up the atomic sample, the dimple trap is ramped on adiabatically. In this process the temperature of the sample nearly stays constant but the Fermi energy increases. With this trick we create a highly degenerate Fermi gas with $T/T_{Fermi} \approx 0.08$ in the dimple [35]. In such a fermionic sample the occupation probability of the lowest energy levels is almost one. We use this high occupation probability in the lowest levels for the preparation of single atoms.

Once the dimple trap is populated, the large dipole trap is switched off so that we retain around 1000 atoms in the tightly focused dipole trap. The free atoms are quickly removed by applying a magnetic field gradient along the top-down axis.

The last step for the deterministic preparation of single atoms is the spilling process. For this we add a magnetic field gradient along the z-direction, which corresponds to the long axis of the microtrap. The total potential in z-direction then given by the optical microtrap which with a Lorentzian profile and the magnetic field gradient. It can be written as

$$V_{tot}(z) = V_{opt}(z) + V_{magn}(z) = pV_0\left(1 - \frac{1}{1 + (z/z_R)}\right) - \mu_m \frac{\partial B}{\partial z} z. \tag{3.4}$$

V_0 is the initial trap depth, p the trap depth parameter and μ_m the magnetic moment of the atom. By tuning the trap depth parameter, we can remove certain atoms from the trap. Figure 3.4(a) illustrates this spilling process. We start from a completely filled microtrap and ramp up a magnetic field gradient to 30 G/cm. This tilts the potentials and creates a potential barrier that allows the atoms on the highest trap levels to escape from the trap. Lowering the power in the trapping beam (this corresponds to decrease the trap depth parameter p) decreases the height of the potential barrier so that more atoms can escape from the trap. For very low beam powers, only the lowest trap levels are populated and all the others escape from the trap. Figure 3.4(b) shows a scan of the beam power, which is directly proportional to the trap depth. Every time, when the potential barrier is lowered below a trap level, all atoms above this level can escape from the trap. This scheme allows us to prepare two atoms in one well with fidelities of around 95%. In addition, by exploiting the different magnetic moments of the hyperfine sublevels, we can even prepare single atoms or imbalanced systems. At a magnetic offset field of $B_{\text{offset}} \approx 27$ G, the magnetic moment $\mu_m = \frac{\partial E}{\partial B}$ of state $|2\rangle$ vanishes (see Fig. 4.4) so that its potential is not affected by the magnetic field gradient. Thus only the other state is removed

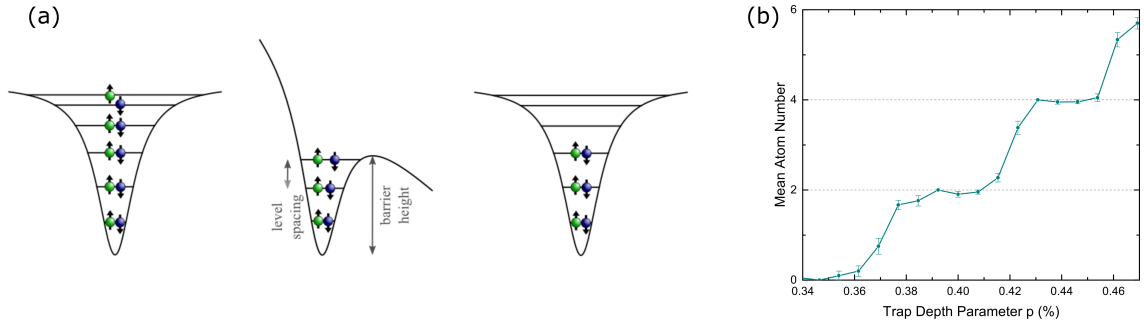

Figure 3.4: (a) In order to deterministically prepare few atoms in the microtrap, the power in the trapping beam is lowered and a magnetic field gradient is applied. The highest atoms are no longer bound and can escape from the trap. Switching off the magnetic field gradient and ramping the power in the trapping beam back to its original value yields a few-atom groundstate system. (b) The plot shows the mean atom number as a function of the trap depth parameter.

by the spilling scheme, leaving a single atom in the trap.

We cannot only prepare atoms in a single well with this technique. As is indicated in Figure 3.5, we use an accousto-optical deflector (AOD) in front of the objective. The AOD consists of a crystal whose density can be periodically modulated by applying an RF-frequency to a piezo element. The light that passes through the crystal is deflected by an angle that is proportional to the frequency of the RF-signal. By applying two different frequencies to the piezo element, we can deflect the light into two different angles. Focusing these two beams with the objective, a double well potential is created in the focal plane. We can extend this method to more wells to realize a small lattice system in which we can control both the depth and the position of each well individually. This part of the setup is characterized in [36].

3.3.2 Detection of single atoms

At the end of the experimental sequence, we have to read out the quantum state of the system by detecting the number of atoms and their spin state in each well. So far the total atom number has been counted by switching off the microtrap and recapturing all atoms into a MOT, called microMOT. In the microMOT, the atoms are illuminated for about 1 s and the fluorescence signal is focused onto a CCD-camera. The collected signal is proportional to the number of atoms so that we are able to count the number of atoms with high fidelities up to around 20 atoms. The histogram in Figure 3.6 shows the collected fluorescence signal normalized to the atom number. In this data the odd atom numbers appeared less often due to the preparation scheme but we can deterministically prepare any of these atom

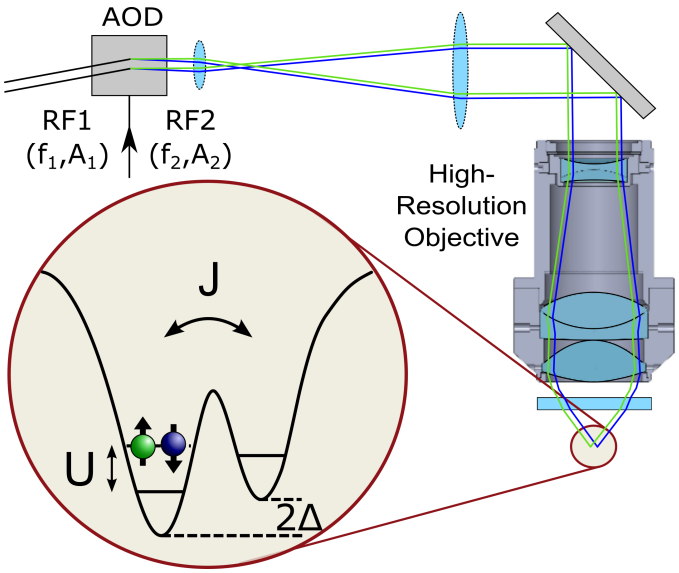

Figure 3.5: The picture above illustrates our method to generate a multiwell potential. We use an AOD to deflect multiple beams in different angles. Focusing for example two beams with our high-resolution objective generates a double well potential in the focal plane. We can control the both the power and the position of each well individually.

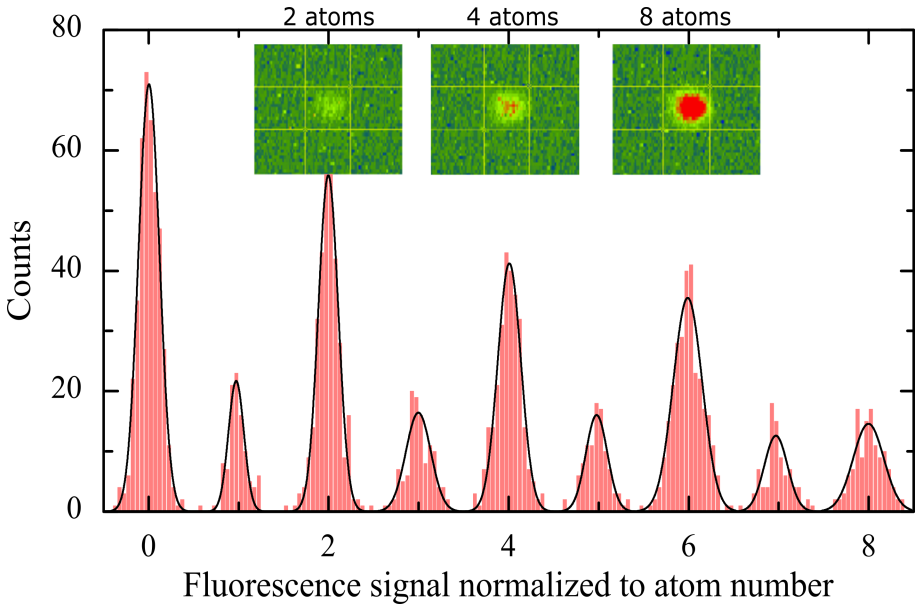

Figure 3.6: For imaging we recapture the atoms from the microtrap into a MOT for around 1 s. By integrating the collected signal, we can count up to 20 atoms with fidelities close to 1. Figure taken and adapted from [33].

numbers. As can also be seen in the Figure, the raw images (single images shown of 2, 4 and 8 atoms) do not contain any information about the well in which the atoms where trapped just before the microtrap was switched off and due to the vanishing magnetic field inside the microMOT, the information about the spin state of the atoms also gets lost. However, exploiting different experimental schemes, we are able to reconstruct the entire state of the system. For example, in order to gain information on the location of the atoms in a double well potential, we first remove the atoms from one well by switching it off. After this, we can count the remaining atom number in the microMOT. By repeating the measurement many times and by employing complex experimental sequences before imaging, we can deduce the quantum state of the system. For larger systems, these detection schemes become very cumbersome so that we aim for a new imaging technique that gives us direct access to the location and the spin state of the atom. This for example enables to directly probe spin-correlations in a multiwell potential.

4 Fluorescence Imaging of ^{6}Li

We illuminate the atoms with sigma-polarized light, resonant to the D_2-transition and collect the fluorescence signal with our high resolution objective. This Chapter will first explain the imaging configuration and then give a detailed analysis of the relevant level structure of ^{6}Li . As will be explained, a deep understanding of the relevant dipole transitions and decay channels is necessary in order to collect enough signal of the atoms without adding a repump-laser. At the end of this chapter, the diffusion of the atom will we simulated numerically and compared to the signal that we measure in the imaging process. In order to prevent the diffusion of the particles during the imaging process, we did measurements where we increased the trap power and compared this to the case where we switched off the trap right before imaging. Both cases are studied at the end of this Chapter.

4.1 Imaging configuration and calibration of the imaging beams

We illuminate the atomic sample from the side with two counterpropagating, horizontally polarized laser beams. We capture the fluorescence photons with a high resolution objective in the vertical direction. Our magnetic field is generated by a pair of coils, one sits on top of the vacuum chamber, the other is right below the chamber. Hence the magnetic field points in the vertical axis. Since the polarization of the imaging light is perpendicular to the orientation of the magnetic field, the atoms experience both σ_+ and σ_-polarized light as is illustrated in Figure 4.1. We are using two independent imaging beams from the two directions. For this setup we were trying out two different imaging sequences. Either both beams are applied to the atom at the same time or both beams are pulsed alternately. In the first case, since both beams have the same wavelength, the imaging beams create a standing wave pattern, which causes - especially for a dense sample of atoms - peculiar effects which are very hard to understand. In the other case, the beams are not overlapping in time, so that the behavior of the atoms is much easier to understand and

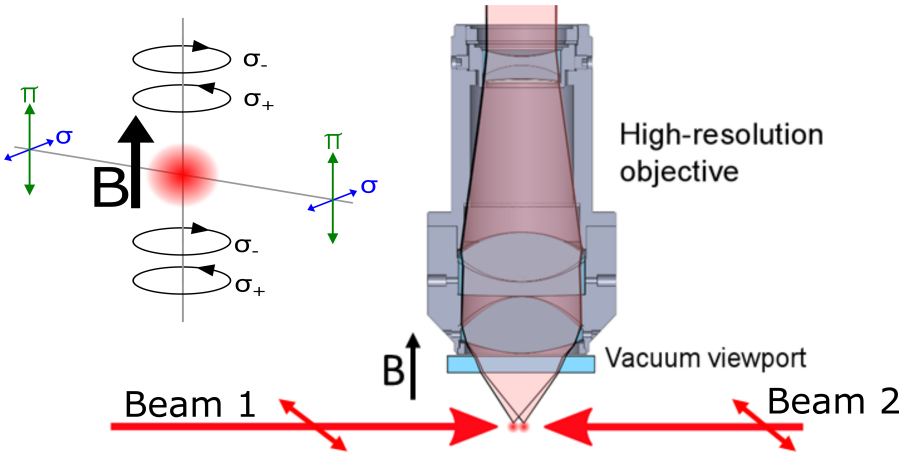

Figure 4.1: We image the atoms with two horizontally polarized laser beams in one axis. The imaging beams are perpendicular to the magnetic field. Hence the atoms experience both σ_+ and σ_- polarized light.

to describe. Figure 4.2(a) illustrates the described imaging sequence, where only one beam is switched on at a time. The first imaging pulse has a length of $1\,\mu$s[1] and the subsequent pulses all have a length of $2\,\mu$s. The typical trap depths of the experiment are so shallow that the confining potential does not hinder the atoms from diffusing. Hence we typically switch off the trapping beam before the imaging process. However we also tried to increase the trap depth for the imaging process. These two cases will be analyzed at the end of this chapter.

The intensity of the two imaging beams was calibrated by measuring the power broadening of the D_2-transition. The scattering rate for an ensemble of identical two level atoms is given by [37]

$$\gamma_{sc} = \frac{s_0\Gamma/2}{1 + s_0 + \left(\frac{2\delta}{\Gamma}\right)^2} \tag{4.1}$$

with $s_0 = I/I_{sat}$, δ the detuning and Γ the natural linewidth of the optical transition. By increasing the imaging intensity s_0, the atomic absorption curve gets power broadened with a linewidth of

$$\Gamma' = \Gamma\sqrt{1 + s_0}. \tag{4.2}$$

For the calibration of the imaging beams, we image an atomic sample at low density[2] for only $1\,\mu$s. The short imaging time is necessary to prevent a line broadening due

[1] This is the shortest timescale of our experiment.
[2] We prepared 50 atoms in our micro trap and let them expand for 50 ms

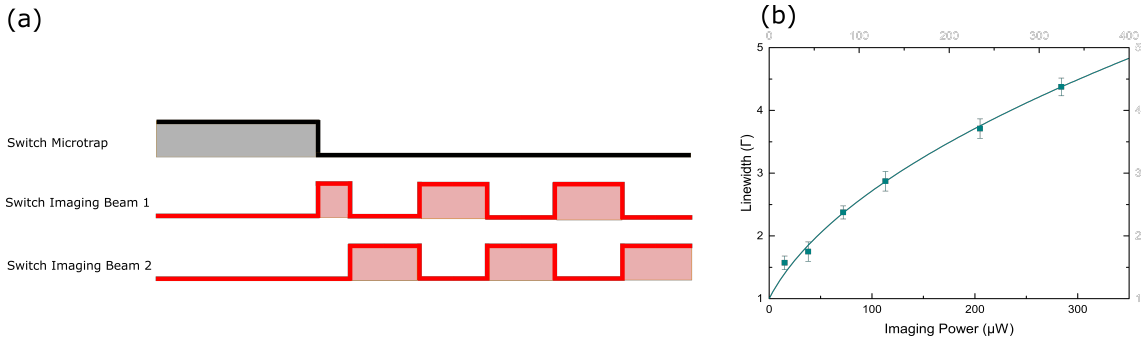

Figure 4.2: (a) illustrates the imaging sequence. Instead of retroreflecting the imaging beam, we use two different beams in order to pulse them alternately from both sides. This imaging sequence does not produce a standing wave interference pattern at the position of the atoms. We start with a first imaging flash of 1 μs from one site. The subsequent flashes are applied for 2 μs. The plot in (b) shows the calibration of the imaging power.

to the acceleration of atoms during the imaging process. By scanning the detuning of the imaging laser, we can measure the linewidth of the transition for different imaging powers. Figure 4.2(b) shows the measured linewidths for different imaging powers. By fitting Equation 4.2 to the data we can deduce the power that is needed in the imaging beam to get the saturation intensity at the position of the atoms.

$$\begin{aligned} P_{Sat}^{Front} &= 28.3 \pm 2.3\,\mu\text{W} \\ P_{Sat}^{Back} &= 15.6 \pm 0.5\,\mu\text{W}. \end{aligned} \tag{4.3}$$

The difference in the saturation power that might be caused by the different beam diameters of the two imaging beams due to a different collimation. These values agree with our estimations of the imaging intensity that we calculated from the measured beam size of the imaging beams. For the chosen configuration of alternating imaging flashes we want to have the maximum scattering rate since the "temperature" of the atoms is much too low for any kind of cooling mechanism. For $s_0 \gg 1$, the scattering rate in Equation 4.1 saturates to $\Gamma/2 = 18.45\,\mu\text{s}^{-1}$.

In order to verify whether we achieve the maximum scattering rate, we measure the average momentum transfer within 1 μs by illuminating the atoms with one imaging beam for 1 μs, letting them expand for several μs and then pulse the same imaging beam again for 1 μs. Figure 4.3 illustrates the atomic sample at different flight times. By fitting gaussians to both the sum in x and y-direction one can deduce the distance that the atoms have traveled within 1 μs. Plotting the distance over time,

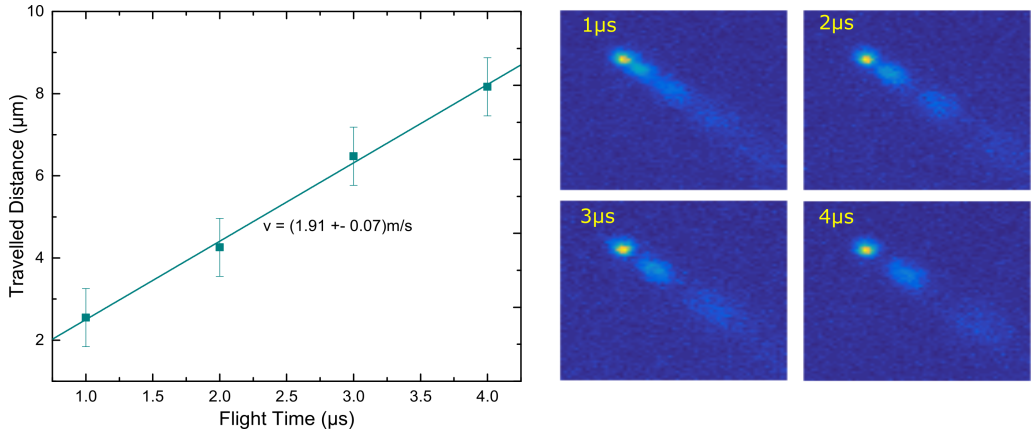

Figure 4.3: The images show the trajectory of the atomic cloud after an imaging pulse of 1 μs. By fitting a gaussian to the signal, we can deduce the momentum transfer and hence the scattering rate.

we can calculate the velocity and the momentum transfer from the laser beam to the atoms. This data was taken at very high imaging power ($s_0 \approx 100$). We measure a momentum transfer of

$$p_{transfer} = (19.3 \pm 1.5)\, \mathrm{p_{photon}}, \tag{4.4}$$

where p_{photon} is the photon momentum for the D_2-line. From Equation 4.1, for $s_0 = 100$ one expects a scattering rate of 18.36 μs^{-1} which agrees with the measured value within the given error. The large error of the measured momentum transfer is not only caused by the fit, it also includes a 5 % error of the magnification which was not exactly known. The uncertainty of the fit was mainly caused by the large spread of the atomic sample after the flight time.

4.2 Level structure of ^{6}Li

^{6}Li has a single valence electron and thus features a simple level structure with a total electronic spin of $s = 1/2$. Hence the ground state of ^{6}Li is $^2S_{1/2}$. For imaging on the D_2 line, we drive the dipole transition ($\Delta J = 1$) into the state $^2P_{3/2}$. The energy splitting to state $^2P_{1/2}$ is around 63 GHz, so that the D_1 and the D_2 transitions do not overlap. Things become a little more complicated, when the hyperfine coupling of the nuclear spin of $I = 1$ to the total angular momentum $\vec{J} = \vec{S} + \vec{L}$ is taken into account. Even though, the angular momentum and the nuclear spin decouple at magnetic field strengths of a few gauss, we need a deep understanding of the level structure in order to explain the temporal evolution of the fluorescence signal for

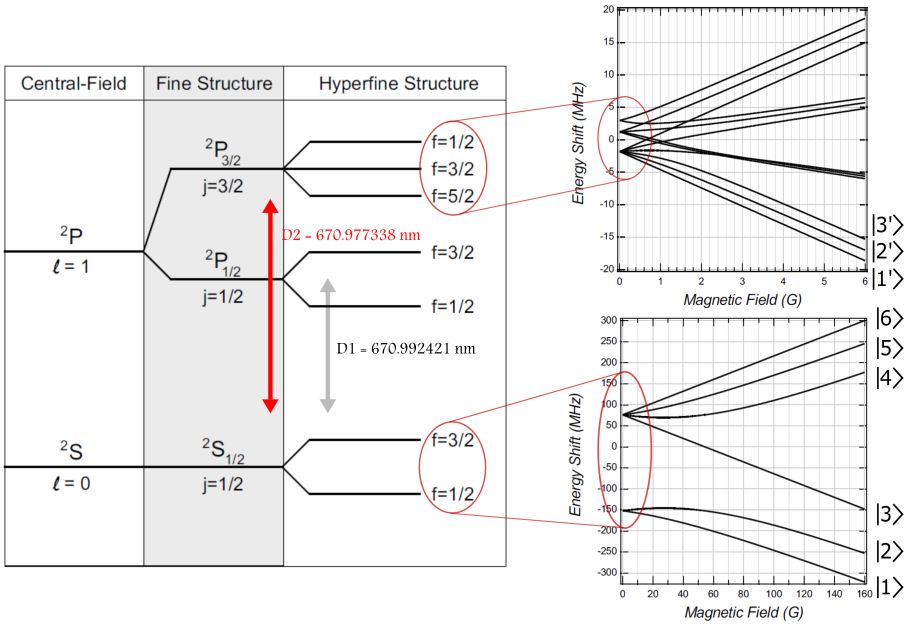

Figure 4.4: The left picture shows the level structure of the lowest levels of ^{6}Li with the fine and hyperfine splitting at no magnetic field. The graphs on the right side show the splitting of the different hyperfine states as a function of the magnetic field. The ground state splits into 6 Zeeman sub levels which we label states 1 to 6 with increasing energy. Figure taken and adapted from [31].

the different hyperfine levels of the ground state.

As shown in Figure 4.4, without a magnetic field, the ground state $^2S_{1/2}$ splits into two hyperfine states with a total angular momentum of $F = \{1/2, 3/2\}$. The splitting between these two substates is around $\Delta E_{GS}^{HF} = 228.2\,\text{MHz} \approx 39\Gamma_{D_2}$. This splitting is very large compared to the hyperfine splitting of the excited state $^2P_{3/2}$. This state splits into three substates with total angular momentum $F = \{1/2, 3/2, 5/2\}$ and a total energy splitting of $\Delta E_{ES}^{HF} = 4.8\,\text{MHz} < \Gamma_{D_2}$.

Each of the hyperfine substates has $2F+1$ different m_F Zeeman sublevels that split up if a magnetic field is applied. Hence at zero magnetic field, the ground state is sixfold degenerate and the relevant excited state twelvefold respectively.

Without an external magnetic field, the total angular momentum F and the magnetic quantum number m_F are valid quantum numbers and characterize the eigenstates of the atom.

^{6}Li in an external magnetic field

Also for small magnetic fields, i.e. in the linear Zeeman-regime, F is still a good quantum number. Hence all substates of both the ground and excited state split up

linearly according to their magnetic quantum number m_F [31]

$$\Delta E_{Zeeman} = \frac{\mu_B}{\hbar} g_F m_F B \tag{4.5}$$

with the Bohr magneton μ_B, the magnetic field B and the g-factor

$$g_F = g_J \frac{F(F+1) - I(I+1) + J(J+1)}{2F(F+1)} + g_I \frac{F(F+1) + I(I+1) - J(J+1)}{2F(F+1)}. \tag{4.6}$$

As the magnetic field increases, the magnetic field energy becomes comparable to the hyperfine energy and F ceases to be a valid quantum number. This causes a decoupling of the nuclear spin I from the angular momentum J and a bending of the energy levels in Figure 4.4(b) with increasing magnetic field. The decoupling of the nuclear spin and the angular momentum already happens on the order of 1 G for the excited state and on the order of $10 - 20$ G for the ground state respectively. In this regime, the eigenstates of the system can best be described in the $|m_J, m_I\rangle$-basis. For the ground state, the six sublevels can be written in an analytic form [31] with B-field dependent prefactors.

$$\begin{aligned}
|1\rangle &= A_+ \,|1/2, 0\rangle - B_+ \,|-1/2, 1\rangle \\
|2\rangle &= A_- \,|1/2, -1\rangle - B_- \,|-1/2, 0\rangle \\
|3\rangle &= |-1/2, -1\rangle \\
|4\rangle &= B_- \,|1/2, -1\rangle - A_+ \,|-1/2, 0\rangle \\
|5\rangle &= B_+ \,|1/2, 0\rangle - A_- \,|-1/2, 1\rangle \\
|6\rangle &= |1/2, 1\rangle
\end{aligned} \tag{4.7}$$

with $A_\pm = 1/\sqrt{1 + (Z^\pm + R^\pm)^2/2}$, $B_\pm = \sqrt{1 - A_\pm}$, $Z^\pm = (\mu_n + 2\mu_e)B/A_{2^2S_{1/2}} \pm 1/2$ and $R^\pm = \sqrt{(Z^\pm)^2 + 2}$, $A_{2^2S_{1/2}} = 152.1368407$ MHz is the magnetic dipole constant, $\mu_{n/e}$ the magnetic moment of the neutron and electron respectively. The states are labeled according to their energy where $|1\rangle$ is the lowest lying state. The right graph in Figure 4.4 identifies the six different states from Equation 4.7.

Our experiment is conducted with the three lowest states, i.e. $|1\rangle, |2\rangle, |3\rangle$. Hence we need to analyze the optical transitions starting from these three states, which will be done in the next section.

In higher magnetic fields, i.e. beyond the linear Zeeman-regime, the nuclear spin I and the angular momentum of the electron J decouple further so that the spitting is governed by the strongest $\{m_J, m_I\}$ component. In this regime, the energy splitting

between two neighboring states is on the order of 80 MHz $\approx 14\Gamma_{D_2}$ so that we can individually address the different spin states by tuning the imaging laser resonant to the corresponding transition. This means that in Equation 4.7, the value for $A_\pm$ decreases and converges towards zero with increasing magnetic field.

$$\begin{aligned}
|1\rangle &\rightarrow |-1/2, 1\rangle \\
|2\rangle &\rightarrow |-1/2, 0\rangle \\
|3\rangle &= |-1/2, -1\rangle \\
|4\rangle &\rightarrow |1/2, -1\rangle \\
|5\rangle &\rightarrow |1/2, 0\rangle \\
|6\rangle &= |1/2, 1\rangle
\end{aligned} \tag{4.8}$$

Figure 4.5 shows the evolution of the coefficients $A_\pm$ and $B_\pm$ of the ground state in (a) and for the excited state in (b). The energy of the states in Equation 4.8 shift linearly with the magnetic field again and arrange according to the main m_J-value as can be seen for high magnetic fields in Figure 4.4.

There is no analytic form for the different levels in the excited state. The qualitative behavior is the same as in the ground state except that the decoupling happens at a much lower magnetic field. This is caused by the angular momentum of $L = 1$ which keeps the electron far from the nucleus. As will be explained in the next section, we only need to consider the three lowest levels of the excited state which we can write in a similar form as we wrote for the ground state.

$$\begin{aligned}
|1'\rangle &= |-3/2, -1\rangle \\
|2'\rangle &= a_2\,|-3/2, 0\rangle + b_2\,|-1/2, -1\rangle \\
|3'\rangle &= a_3\,|-3/2, 1\rangle + b_3\,|1/2, -1\rangle + c_3\,|-1/2, 0\rangle
\end{aligned} \tag{4.9}$$

where a, b, c are the field coefficients that are illustrated in Figure 4.5(b). Again the states are labeled with increasing energy. Already in magnetic fields on the order of 10 G the angular momentum and the nuclear spin start to decouple so that for fields around 500 G we can write the states as

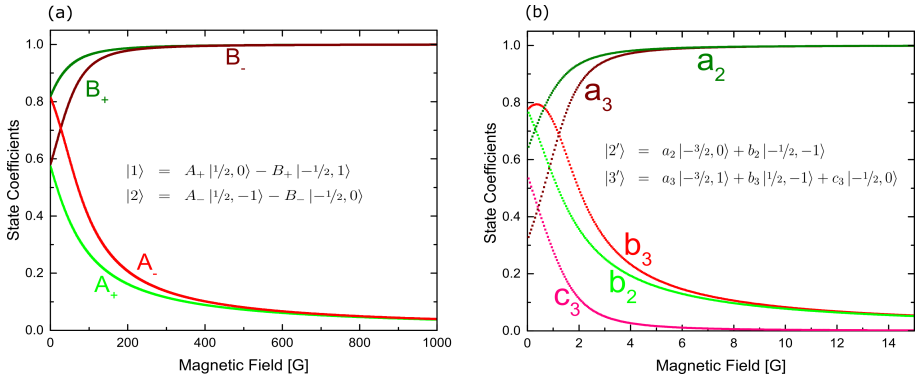

Figure 4.5: The graphs show the coefficients of states $|1\rangle$ and $|2\rangle$ of the ground state from 0 G to 1000 G and $|2'\rangle$ and $|3'\rangle$ of the excited state from 0 G to 15 G. For increasing magnetic fields the angular momentum of the electron decouples from the nuclear spin such that only one coefficient survives. This happens much faster for the excited state since the mean distance from the electron to the nucleus is much larger than in the ground state.

$$\begin{aligned} |1'\rangle &= |-3/2, -1\rangle \\ |2'\rangle &\rightarrow |-3/2, 0\rangle \\ |3'\rangle &\rightarrow |-3/2, 1\rangle \,. \end{aligned} \tag{4.10}$$

However, even if the spins decouple and the states of both the ground and the excited state can well be described as above, there is always a small admixture of another state as is known from Equation 4.7. These admixtures of other states influence the optical transition as will we see in the next chapter.

4.3 Dipole transitions in the imaging process

In order to understand the transitions during the imaging process, let us start at very high magnetic field and assume, that the states can be written in the forms of Equations 4.8 and 4.10 respectively, i.e. we only consider the main m_J contribution for now. Figure 4.6(a) attributes the main m_J values to the different manifolds in both the ground and the excited state. Starting from the three lowest levels of the ground states, σ_--polarized light brings us into the lowest manifold of the excited state. Since π polarized light does not change the m_J value, it excites the atom into the second lowest manifold. Hence, σ_+-polarized light excites the atoms into the $m_J = +1/2$ manifold. At our typical magnetic fields, the splitting of the different

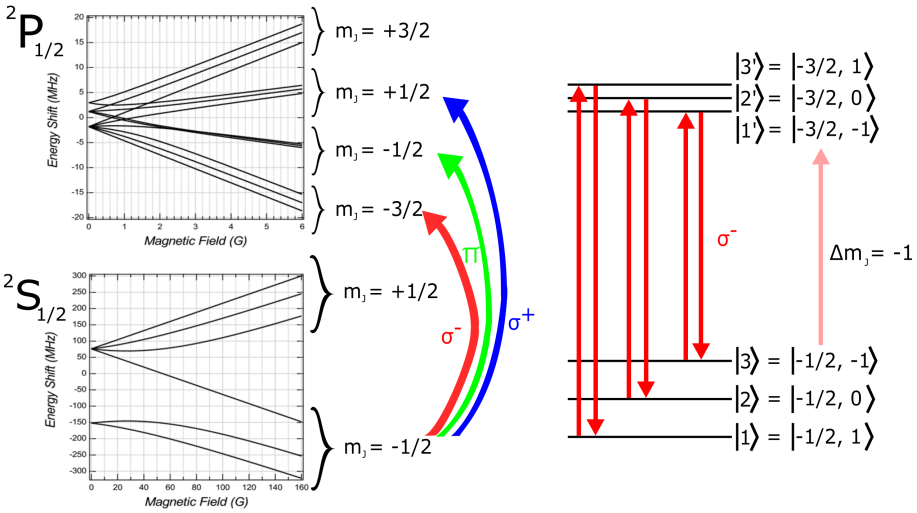

Figure 4.6: In very high magnetic fields the angular momentum of the electron decouples from the nuclear spin. In this regime, the states can well be described by the quantum number m_J. The left plot shows the possible dipole transitions for different polarizations of the imaging light and the right graph shows a zoom into the σ_- transition. From the excited state, the atom can only decay into its original state since $\Delta m_J = +1$ and $\Delta I = 0$ has to be fulfilled.

manifolds in the excited states is on the order of some GHz, so that we can select the different manifolds in the excited state by tuning the laser resonant to the according transition. In the experiment we image into the lowest, i.e. the $m_J = -3/2$ manifold so that we only need to consider the three lowest sublevels of the excited state. We can apply the selection rules for σ_- polarized light to the three lowest hyperfine sublevels of the ground state and find the transitions as indicated in Figure 4.6(b). The decay always happens into the initial state, since the orientation of the nuclear spin does not change during the imaging process.

As explained in the previous section and as shown in Figure 4.5, $|1\rangle$ and $|2\rangle$ of the ground state and states $|2'\rangle$ and $|3'\rangle$ of the excited state do have small but finite admixtures of other spin states which need to be included into the analysis of the dipole transitions. State $|3\rangle$ of the ground state and state $|1'\rangle$ of the excited state do not have any admixture of other states. This is due to the fact that the angular momentum $\vec{J}$ of the electron points in the same direction as the nuclear spin $\vec{I}$. For this reason the magnetic moment of these both states is $\mu = \frac{\partial E}{\partial B} = const$ and the energy shifts linearly with the magnetic field in all regimes. As already explained, the convergence of the coefficient of the main m_J state is much faster in the excited state than in the ground state. Hence for typical magnetic fields above 500 G, we

can use the form of Equation 4.10 for the excited state[3].
However, for the ground state, we need to take the full form into account since even a very small residual other spin state causes significant loss during the imaging process. In the following, we first analyze the excitation from the three different levels in the ground state $|1\rangle, |2\rangle, |3\rangle$ and then the spontaneous decay from the corresponding excited states.

Excitation from the ground state

As explained in section 4.1, the imaging light is linearly polarized in the horizontal plane. The magnetic field is pointing in z-direction. Hence the polarization is orthogonal to the magnetic field such that the atoms experience both σ_+ and σ_- polarized light. Since our laser beam is tuned resonant to the σ_- transition, we need the selection rule for the excitation of an electron from the ground state

$$\Delta J = 1, \Delta m_J = -1, \Delta m_I = 0. \tag{4.11}$$

With these selection rules in the $|m_J, m_I\rangle$ basis, let us now analyze the full form of the ground state levels $|1\rangle$ and $|2\rangle$ that was given in Equation 4.7. Both of these states have one main m_J value which was already analyzed above and one secondary m_J value that still needs to be taken into account.
Table 4.1 analyzes the three different sublevels of the ground state separately. The J-selection rules from above are applied to each of the admixtures to see into which m_J-states an excitation is possible. Then these m_J- states are compared to the different levels in the excited state from Equation 4.9 to find the final state after the transition. The final state can be found in the last column. Fortunately the large detuning to the σ_+ and the π transitions to the excited state restrict each level from the ground state to only one level in the excited state when σ-polarized light is used. Hence no atoms can get lost or dark during the excitation with σ-polarized light.
However, one should note that also π-polarized light can also drive a transition into the lowest manifold of the excited state, if the full form of the excited state is considered. There are two possible π transitions within the σ_- transition.

$$|2\rangle \rightarrow |3'\rangle, |3\rangle \rightarrow |2'\rangle \tag{4.12}$$

However, the probability for such transitions is on the order of 10^{-12} and can there-

[3]E.g. at 500 G, State 2 has admixtures $b_2 = 1.3 \times 10^{-6}$, $1 - a_2 = 1.15 \times 10^{-6}$.

Initial State	Admixtures	State after applying $\Delta m_J = -1$	Final state within $m_J = -3/2$ manifold
$\|1\rangle$	secondary: $\|1/2, 0\rangle$	$\|-1/2, 0\rangle$	$\|3'\rangle$
	main: $\|-1/2, 1\rangle$	$\|-3/2, 1\rangle$	$\|3'\rangle$
$\|2\rangle$	secondary: $\|1/2, -1\rangle$	$\|-1/2, -1\rangle$	$\|2'\rangle$
	main: $\|-1/2, 0\rangle$	$\|-3/2, 0\rangle$	$\|2'\rangle$
$\|3\rangle$	$\|-1/2, -1\rangle$	$\|-3/2, -1\rangle$	$\|1'\rangle$

Table 4.1: Excitation from the ground state with σ-polarized light: The first column shows the three different levels of the ground state. If the selection rules from Equation 4.11 are applied, each admixture from the second column can be excited into two different states. The fourth column shows the resonant transitions so that in the last column the final state is identified.

fore be neglected. Furthermore in the experiment we ensure with polarizing beam splitter cubes, that there is no π polarized light in the imaging beams.

Decay from the excited state

As already argued above, we can approximate the levels in the excited states with Equation 4.10.

$$\begin{aligned} |1'\rangle &= |-3/2, -1\rangle \\ |2'\rangle &= |-3/2, 0\rangle \\ |3'\rangle &= |-3/2, 1\rangle \end{aligned} \tag{4.13}$$

These states can only decay by emitting σ_--polarized light since there is no state with $m_J = -3/2$ available in the ground state. We can apply the selection rules from Equation 4.11 in a reverse fashion and write the output as a superposition of the different levels in the ground states

$$\begin{aligned} |1'\rangle &= |-3/2, -1\rangle \to |-1/2, -1\rangle = |3\rangle \\ |2'\rangle &= |-3/2, 0\rangle \to |-1/2, 0\rangle = -B_- |2\rangle - A_- |4\rangle \\ |3'\rangle &= |-3/2, 1\rangle \to |-1/2, 1\rangle = -B_+ |1\rangle - A_+ |5\rangle . \end{aligned} \tag{4.14}$$

This shows, that for σ-polarized light we have a completely closed transition for

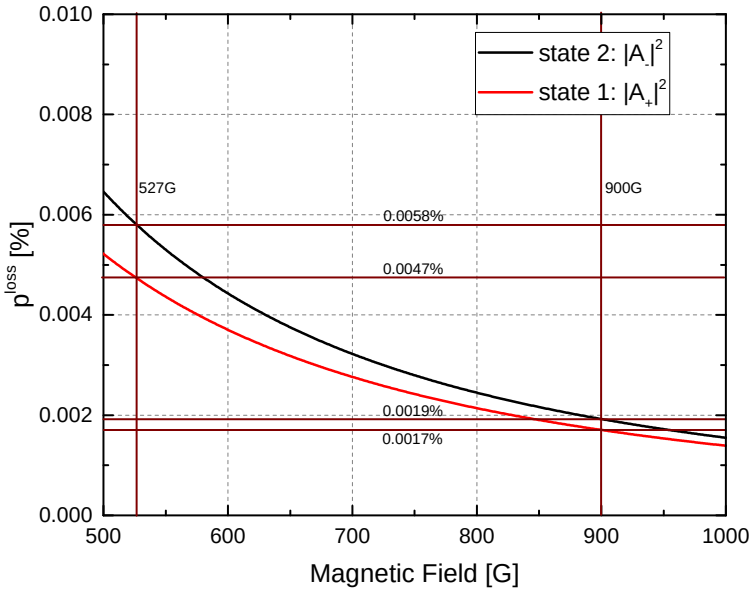

Figure 4.7: The graph above shows the probability for both state $|1\rangle$ and state $|2\rangle$ to get lost into a non-resonant state (states $|5\rangle$ and $|4\rangle$). Once the atoms decays into one of these states, they do no longer scatter photons and we therefore might not be able to collect enough signal for the detection of the atom.

state $|3\rangle$

$$|3\rangle \rightarrow |1'\rangle \rightarrow |3\rangle\,. \tag{4.15}$$

The two other levels of the ground state do not have a completely closed transition

$$\begin{aligned} |1\rangle &\rightarrow |3'\rangle \rightarrow -B_+\,|1\rangle - A_+\,|5\rangle \\ |2\rangle &\rightarrow |2'\rangle \rightarrow -B_-\,|2\rangle - A_-\,|4\rangle\,. \end{aligned} \tag{4.16}$$

After one cycle the excited state can decay into states $|5\rangle$ or $|4\rangle$ with probabilities $p^{loss}_{|1\rangle} = |A_+|^2$ and $p^{loss}_{|2\rangle} = |A_-|^2$ respectively. This probability is plotted in Figure 4.7. In the plot, two magnetic fields are marked, 527 G, where the s-wave scattering length of states $|1\rangle$ and $|2\rangle$ vanishes and 900 G. At these magnetic field strengths, the probability to decay into the non resonant state is

$$\begin{aligned} p^{loss}_{|1\rangle}(527) &= 0.47\% \\ p^{loss}_{|2\rangle}(527) &= 0.58\% \\ p^{loss}_{|1\rangle}(900) &= 0.17\% \\ p^{loss}_{|2\rangle}(900) &= 0.19\% \end{aligned} \tag{4.17}$$

This means that we can close the optical transitions of the sublevels $|1\rangle$ and $|2\rangle$ by increasing the magnetic field. These two values were measured in the experiment for state 2 and will be presented in the next section.

4.4 Dipole radiation pattern

The magnetic field not only influences the available atomic dipole transitions, it also has an effect on the spatial radiation pattern of the atom. The magnetic field, which is pointing in the vertical direction, polarizes the atom. This effect enhances the emission of photons into the direction of the objective.
As explained, the atom can only emit σ_+ polarized light when decaying from the excited state into the ground state. Thus the atoms radiate according to the dipole radiation pattern [38]

$$\hat{\mathrm{I}}(\theta) = \frac{I(\theta)}{I_0} = \frac{3}{16\pi}\frac{(1+\cos^2\theta)}{2}. \tag{4.18}$$

The factor of $\frac{3}{16\pi}$ is a normalization factor so that the integral over the whole solid angle is one. Thus the total signal S, that is collected by the objective with a numerical aperture of $NA = \sin\alpha$ is given by

$$\begin{aligned} S &= \int_0^{\alpha}\int_0^{2\pi} \hat{\mathrm{I}}(\theta)\sin\theta d\theta d\phi \\ &= 2\pi\int_0^{\alpha} \hat{\mathrm{I}}(\theta)\sin\theta d\theta \\ &= -\frac{3}{8}\int_0^{\alpha}[1+\cos^2\theta]d\cos\theta \\ &= -\frac{3}{8}[\cos\theta + \frac{1}{3}\cos^3\theta]|_0^{\alpha} \\ &= \frac{3}{8}[\frac{4}{3} - \cos\alpha + \frac{1}{3}\cos^3\alpha]. \end{aligned} \tag{4.19}$$

The numerical aperture of our objective is $NA = 2sin(\alpha) \approx 0.55$. This corresponds to an opening angle of $2\alpha = 66.7\,^\circ$ and therefore to a solid angle of $\frac{\Omega}{4\pi} = \frac{1}{2}(1 - cos(\alpha)) = 8.2\%$. However, due to the dipole radiation pattern we collect 11.4 % of the scattered photons. A plot of Equation 4.19 is shown Figure 4.8.
The optical elements that focus the fluorescence light onto the camera cause a loss

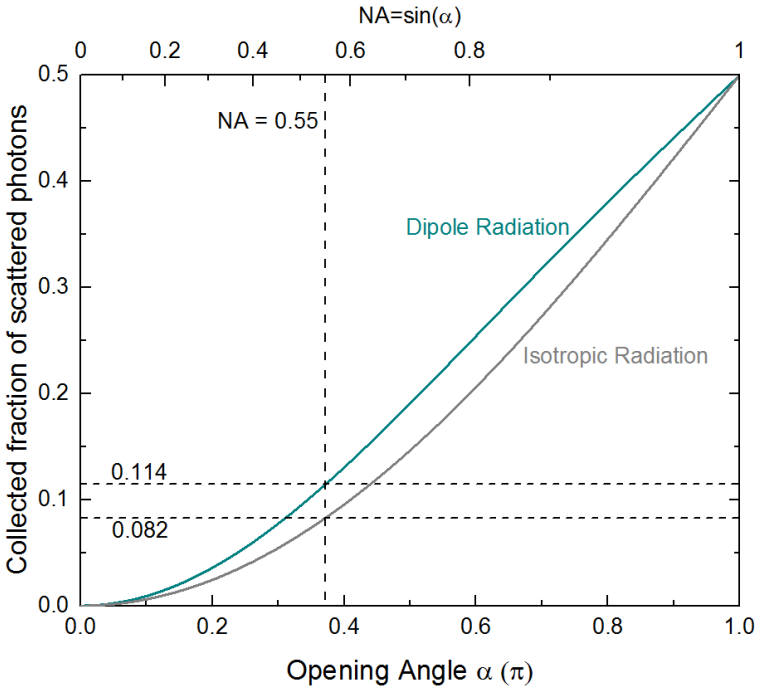

Figure 4.8: The graph illustrates the enhancement of the collected signal due to the dipole radiation pattern from Equation 4.18. For our objective with a numerical aperture of $NA = 0.55$, the dipole radiation increases the signal by 3.2%.

on the order of 10%, such that approximately 10.3 % of the emitted photons impinge on the sensor of the camera. The camera itself has a specified quantum efficiency of 85% at 671 nm, so that 8.7 % of the photons can be detected.
Assuming a near-resonant laser beam, red-detuned by one linewidth from the resonance frequency, with a saturation parameter of $s_0 = {}^{I}/_{I_{sat}} = 100$, the atoms scatter photons according to Equation 4.1

$$\gamma_{sc} = 17.6\,\text{photons}/\mu\text{s} \tag{4.20}$$

With the above parameters, this gives rise to 1.54 detected photons per μs on the camera if the scattering rate stays constant. As explained in the previous section, this is only the case for state $|3\rangle$ since the two other states $|1\rangle$ and $|2\rangle$ decay into non-resonant spin states. This will further be analyzed in the next section.

4.5 Temporal evolution of the fluorescence signal

As we saw in the previous sections, only state $|3\rangle$ features a completely closed transition. The two other spin states $|1\rangle, |2\rangle$ may decay into non-resonant states

($|6\rangle, |5\rangle$). This probability can be decreased by increasing the magnetic field. Since single images of single atoms do not contain enough photons to analyze the temporal increase of the collected signal, we analyze averaged images.
For this, we prepare a single atom in either state $|3\rangle$ or $|2\rangle$ and image it with varying imaging time. State $|2\rangle$ was imaged at two different magnetic fields $B_1 = 527\,\mathrm{G}$ and $B_2 = 900\,\mathrm{G}$. Around 200 images per data point were averaged. We subtract the background from the averaged image and sum up the counts on the camera. From this we can estimate the average number of collected photons by dividing the result by the gain was will be explained in Chapter 5.2.
From the analysis above, we expect that for state $|3\rangle$ the fluorescence signal increases linearly with time. Knowing the approximate scattering rate, this also allows us to determine the total fraction of detected photons by comparing the slope of the signal with the scattering rate. In contrast, for state $|2\rangle$, which does not exhibit a completely closed transition, we expect a saturation of the average fluorescence signal. However, the saturation should be slower for higher magnetic fields.

For a state that decays into a non-resonant state with a probability p and initially scattered photons with the rate γ, the population in the initial state evolves as

$$\mathscr{P}(t) = (1-p)^n = (1-p)^{t\gamma}, \tag{4.21}$$

with n being the number of scattered photons. Hence, the average collected fluorescence signal $\mathscr{S}(t)$ on the camera is given by the integral of the time dependent scattering rate

$$\mathscr{S}(t) = \mathscr{F}\gamma \int_0^t \mathscr{P}(t')dt' = \frac{(1-p)^{t\gamma} - 1}{\log(1-p)}. \tag{4.22}$$

$\mathscr{F}$ is the detection fidelity of a photon with the camera.

Figure 4.9 shows data for state $|3\rangle$ and for state $|2\rangle$ at two different magnetic fields. The black data belongs to state $|3\rangle$ and can be fit with a linear model. Using the slope of the fit of $a = 1.65\,\mathrm{photons}/\mu\mathrm{s}$, and a scattering rate of $\gamma = 17.6\,\mathrm{photons}/\mu\mathrm{s}$[4], we can estimate the detection fidelity to be

$$\mathscr{F} = \frac{1.65 \pm 0.03}{17.6 \pm 0.9} = 9.4 \pm 0.5\% \tag{4.23}$$

[4]The experiment was done with $I_{img} \approx 100 I_{Sat}$ and at a detuning of almost one linewidth. This corresponds to a scattering rate of $\gamma = 17.6\,\mathrm{photons}/\mu\mathrm{s}$

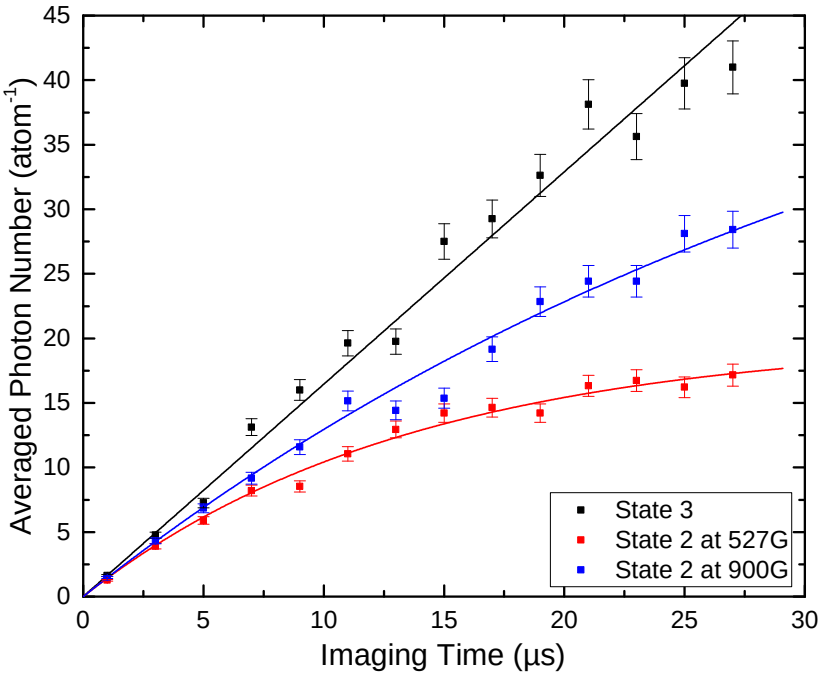

Figure 4.9: The graph above shows the temporal evolution of the collected fluorescence signal for state $|3\rangle$ and $|2\rangle$ at 527 G and 900 G. Due to the completely closed optical transition of state $|3\rangle$, the signal increases linearly while the signal of state $|2\rangle$ saturates. For a higher magnetic field, this saturation takes longer.

The uncertainty of the detection fidelity is taken from the fit. For the scattering rate an uncertainty of around 5 % was assumed. This value is slightly above the estimation that was done with Equation 4.19. The reason for this might be a slightly higher numerical aperture of our objective than $NA = 0.55$.
We fix the detection fidelity to this value since it is needed for fitting the remaining data with Equation 4.22. The red and the blue data points in the figure correspond to state $|2\rangle$ at 527 G and 900 G respectively. Fitting Equation 4.22 to the data yields a scattering rate of $\gamma_{fit} = 15.7 \pm 0.7\,\text{photons}/\mu\text{s}$. From the fits, we extract the probability p for state $|2\rangle$ to decay into the non-resonant spin state $|4\rangle$

$$\begin{aligned} A_{527}^{exp} &= (1-p) = (99.53 \pm 0.02)\,\% \\ A_{900}^{exp} &= (1-p) = (99.83 \pm 0.02)\,\%. \end{aligned} \tag{4.24}$$

The given error is only the 1σ uncertainty of the fit but it does not include the uncertainty of the scattering rate or the detection probability. From section 4.3 and from Figure 4.7 we expect probabilities of

$$\begin{aligned} A_{527}^{th} &= 99.42\,\% \\ A_{900}^{th} &= 99.81\,\%. \end{aligned} \tag{4.25}$$

Keeping in mind that these numbers only include σ-polarized light with the correct detuning and that both the scattering rate and the detection fidelity are not exactly known, the measured values agree very well with the expectations. For even higher magnetic fields, the average signal of the atoms increases even further so that at high magnetic field also states $|1\rangle$ and $|2\rangle$ can be imaged with an almost closed optical transition.

4.6 Diffusion during the imaging process

As explained at the beginning of this chapter, each imaging flash, except the first one, is $2\,\mu$s long. The alternating imaging technique causes the atom to oscillate along the beam axis. According to Equation 4.1, an intensity of $s_0 \approx 100$ and a detuning of one linewidth corresponds to a scattering rate of $\gamma \approx 17.6\,\text{photons}/\mu\text{s}$. The absorbed photons are isotropically emitted in the polar angle ϕ. In θ-direction, the emission happens according to Equation 4.18. With these assumptions we can perform a Monte-Carlo simulation of the trajectory of the atom. For this a mean scattering rate of $\gamma = 17.6\,\mu\text{s}^{-1}$ with a width of $\delta\gamma = 1\,\mu\text{s}^{-1}$[5] is assumed. Each photon is emitted according to the dipole radiation pattern and the momentum is projected onto the plane in which the atoms are imaged. Figure 4.10 shows the temporal evolution of the particle-trajectory in the xy-plane in both axes, along the imaging beam (a) and perpendicular to the beam (b) within an imaging time of $20\,\mu$s. For the simulation, a $1/e^2$ trap diameter of $1.3\,\mu$m was assumed. This corresponds to an harmonic oscillator length of $a_{HO} = 0.5\,\mu$m. Along the beam axis, already after $5\,\mu$s, the diffusion due to the random emission dominates the oscillation that is caused by the imaging technique. Obviously, the spread of the atomic distribution along the imaging beam is larger than the perpendicular spread. Shorter imaging pulses should produce a smaller signal on the camera and thus improve the resolution of the imaging process. Below the images with the simulation, the temporal evolution of the fluorescence signal is illustrated. The graphs correspond to the sum of the images along the time-axis up to different imaging times. Due to the diffusion, the

[5] This has been estimated from the variance of the time for being in the excited state. For this an exponentially decaying probability with a $1/e$-time of Γ^{-1} was used.

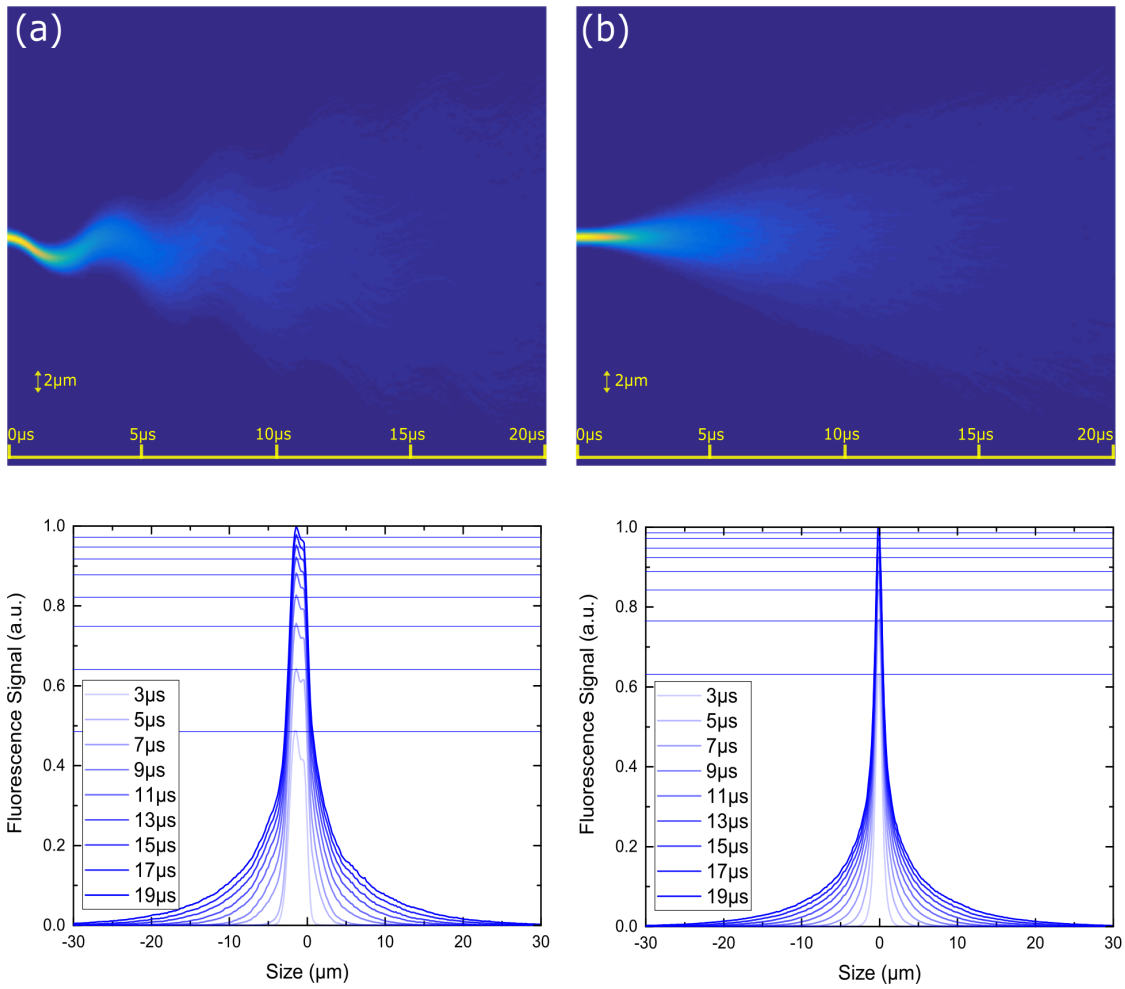

Figure 4.10: The images show a simulation of the diffusion of the atom during the imaging process both along the beam axis (a) and perpendicular to it (b). The graphs below show the spread of the collected signal on the camera. They have been obtained by integrating the images along the time axis for different imaging times.

maximum height of the signal saturates for longer imaging times in both axes and the signal gets accumulated in the wings of the distribution. This saturation is indicated by the horizontal lines in the plots which always mark the peak height. Already after around 7 μs, the increase of the signal is small compared to the spread of the atomic distribution. A longer imaging times can indeed increase the number of collected photons but the signal gets more and more accumulated in the wings. Hence, for a multi-well potential this would decrease the contrast of neighboring wells.

We compare these calculations to averaged images of single atoms. For an averaged image, one expects a slightly elongated signal along the imaging beam. Figure 4.11(a) shows 4 such images. They were obtained by averaging around 150 raw images of single atoms. Each image is normalized to its peak value. The imaging time is always indicated on the image. The imaging beams are pointing along the diagonal direction[6]. In the images, one can see the diffusion of the particles away from their initial position, with a larger spread along the imaging beam axis. The graph in (b) analyzes the temporal evolution of the signal within a specified region of interest. For simplicity we choose only the brightest pixel of the averaged image which corresponds to a size of $2.7 \times 2.7\,\mu\text{m}^2$ in the focal plane. For the comparison we integrate the spatial profiles from Figure 4.10 for different imaging times over the size of a single pixel both along the imaging beam and perpendicular to it. We plot this together with the height of the brightest pixel of the averaged image. Both the experimental data and the simulation have been normalized to the (extrapolated) number of collected photons after an imaging time of 40 μs. The measured data qualitatively agrees very well with the simulation. Hence the simulation describes the diffusion of the atom appropriately.

Another thing that we can compare is the spread of the atomic density distribution. The graphs in 4.12 show the temporal evolution of the signal in the same fashion as was plotted in the graphs in Figure 4.10. Instead of plotting both axes separately, the Figure shows the radial average of the images. This means that the signal is averaged over the whole azimuthal angle ϕ[7] and plotted as a function of the radius. As mentioned above, one pixel of the images corresponds to a size of 2.7 μm in the focal plane. This gives us only a few data points within the signal of the atoms. The first graph in the figure shows the real data and the second plot shows fitted Voigt-profiles without the real data. These describe the data very well and allow to extract the FWHM of the averaged atomic distribution.

[6] Top left corner to bottom right corner
[7] In cylindrical coordinates.

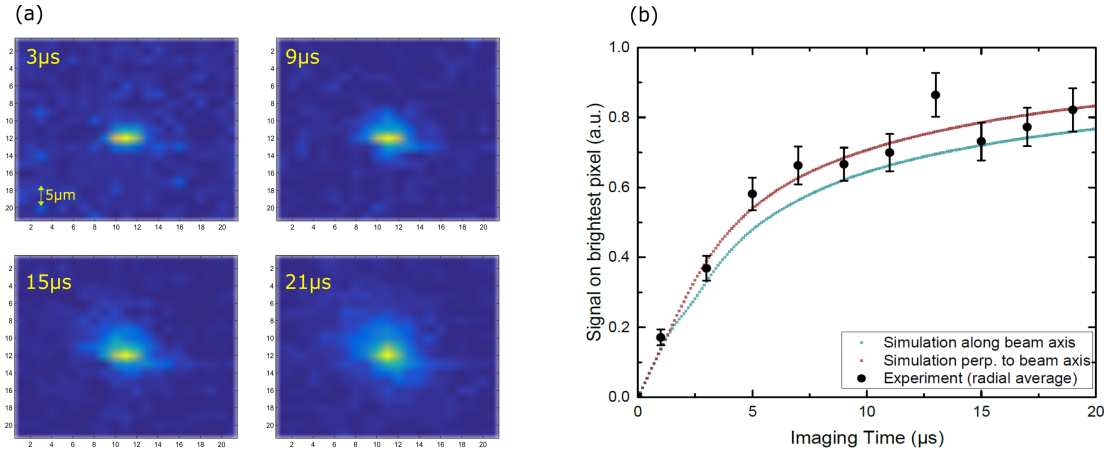

Figure 4.11: The images in (a) are averaged images of single atoms. They illustrate the diffusion of the atomic distribution. The cloud is elongated along the imaging beams (top left corner to bottom right corner). The graph on the right shows a simulation of the evolution of the fluorescence on the brightest pixel both along the imaging beam (green) and perpendicular to it (brown). The black data points are the measured values which we expect to be somewhere between the two simulations. The data qualitatively agrees well with the simulation.

From the fits we get a FWHM after 19 μs of $4.7 \pm 0.5\,\mu$m. From the simulation above we expect a FWHM between 1.9 μm (which is the FWHM perpendicular to the imaging beam) and 3.8 μm (which is the FWHM along the beam). Our measured value is 20 % higher than the simulated value. This can be caused by e.g. a badly focused imaging setup. In fact we will see in Chapter 6 that switching off the imaging beam causes the atoms to delocalize very fast which also broadens the atomic distribution. Hence we can try to counter this delocalization by keeping the trap on during the imaging process.

Not only this delocalization but also the diffusion of the particles will later limit the contrast in the multi-well potential. Hence we try to counter the diffusion by moderately increasing the trapping potential. For this we ramp the laser power in the trapping beams to 10 mW which corresponds to a trap depth of 97.5 μK in the excited state. The recoil temperature of ^{6}Li is $T_{rec} = 3.54\,\mu$K. Hence the trap is around $27.5E_{rec}$. So far we have not really understood what exactly happens to the atom in the trap during the imaging process but the atom cannot leave the trap before it gained at least $28E_{rec}$. For our typical scattering rate of 17.6 μs^{-1}, this means that the atom should be trapped for at least 1.6 μs.

Figure 4.13 shows averaged images for both cases. In the upper images, the trapping

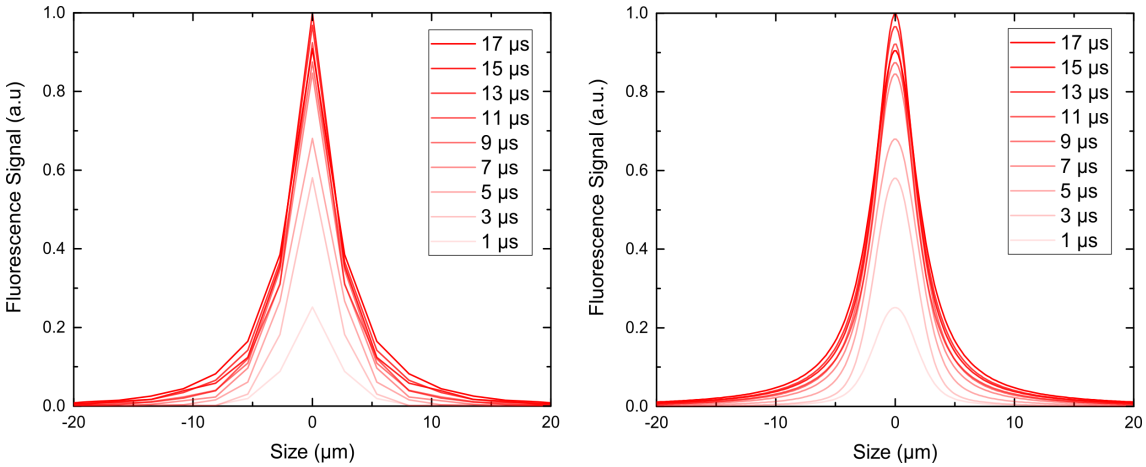

Figure 4.12: The first graph shows the measured radial average of averaged images for different imaging times. The second graph shows fitted Voigt-profiles to determine the FWHM of the distribution.

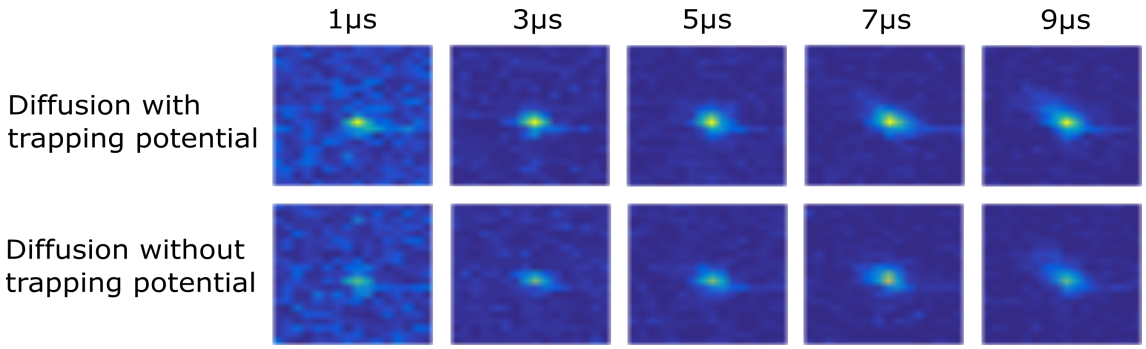

Figure 4.13: The images show that the diffusion of the atom can be countered by ramping deep the trapping potential. For this the laser power in the trapping beams is ramped to 10 mW and kept on during imaging. This depth corresponds to $27.5E_{rec}$ in the excited state. Two images that belong to the same imaging time have the same color scale. The upper images have a more pronounced peak. The reason for this is that as long as the atoms are trapped, the fluorescence signal is focused on the same pixel. Hence the difference of the signal on the central peak gives us information about the time the atom was trapped.

beam is kept on whereas in the lower images the trapping beam is switched off. The scale of the images that belong to the same imaging time is always the same. In the images one can see, that the upper images are much more peaked and have more signal on the brightest pixel.

To compare these two cases, we plot again the signal on the brightest pixel, as was done in Figure 4.11. This is shown in Figure 4.14. The red data points correspond to the case where the trap was switched off before imaging and the cyan data points to the case where we ramped the trap deep. As expected, when the trap is kept on during the imaging process, more signal accumulates on the brightest pixel. As soon as the atoms have enough energy to leave the trap, the signal starts to saturate.

The difference in the signal for imaging with and without trapping potential is the signal that accumulates in the time while the atoms are trapped. We can therefore try to estimate the time the atoms are trapped by comparing the initial slope of the signal to the difference of the accumulated signal. The difference of the two signals is $\Delta = 0.61 \pm 0.10$ photons. This is an increase of more than 50 %! With the initial slope, we can estimate the number of additional scattering events when the atom is trapped during the imaging event. For a lower bound, we choose the larger initial slope of 0.37 photons/μs. Hence the trap keeps the atoms localized for around $\tau = \frac{0.61}{0.37 \mu s^{-1}} = 1.65 \pm 0.38\,\mu$s. This is only a very rough estimation, but this agrees with the estimation of the trap depth.

As was shown in this chapter, we are dealing with very few photons. Hence it is necessary to detect them with a high fidelity. The next chapter describes how we can detect single photons with an EMCCD camera and presents a model to analyze the output of such a camera.

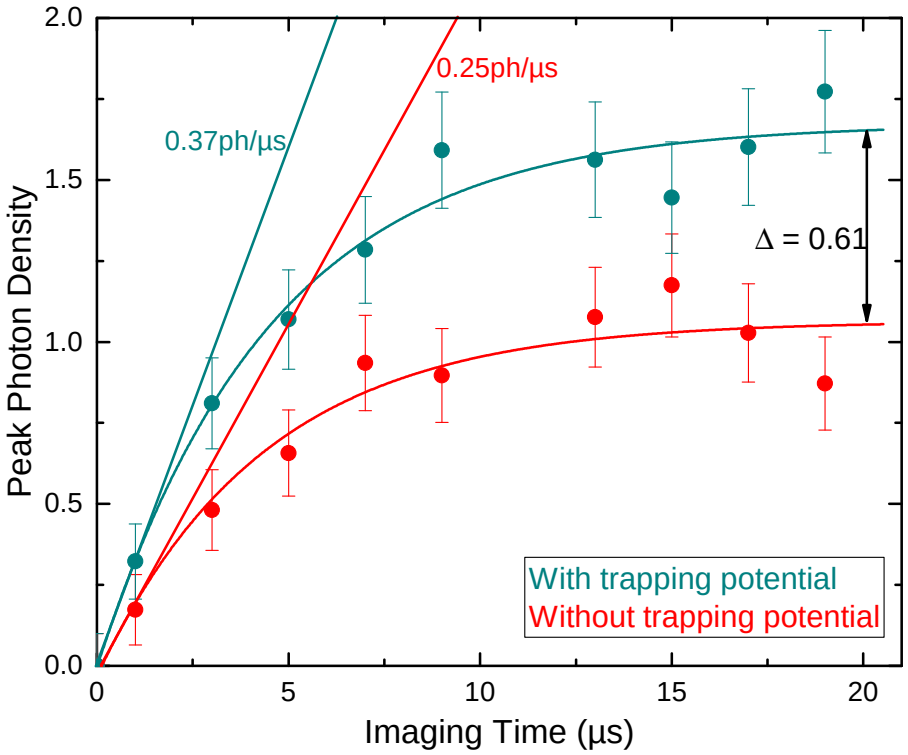

Figure 4.14: The graph plots the signal on the brightest pixel with and without a trapping potential during the imaging procedure. In the case where the trapping beam is kept on, we collect more signal on the brightest pixel. The increase in the signal on the brightest pixel can be used to estimate the time how long the trap keeps the atoms localized. In this run, the trap was ramped to a trap depth of around $27\,\mathrm{E_{rec}}$ which agrees with the increase in the signal.

5 The Detection of Few Photons

Our imaging approach is working in the regime of very few photons. As has been estimated in the previous chapter, we only collect around 10-20 photons per atom. To detect such low photon numbers down to a single photon resolution, we need a high resolution objective and a camera with a high quantum efficiency to detect as many photons as possible. Furthermore it is necessary that one photon creates a signal above the noise level. For these reasons we use a CCD camera with EM-mode (**E**lectron **M**ultiplying **C**harge-**C**oupled **D**evice). This camera amplifies the detected signal before reading it out so that single photons can be detected.
In this chapter, the setup for the detection and the counting of photons is described and characterized. The first part deals with the working principle of an EMCCD-camera and the technical difficulties that come along with it. The different sources of noise are explained and analyzed. In the second part our camera is characterized by analyzing the gain and the different sources of noise. The results of these measurements are compared to the values that are specified by Andor.

5.1 Properties of an EMCCD camera

A CCD-sensor is a device that produces electrical charges from incident photons and converts them into a digital signal. It consists of a photoactive layer of silicon on top of a capacitor array. Figure 5.1 illustrates the basic principle of a CCD-sensor. During the imaging acquisition, the impinging photons create photoelectrons inside the photoactive layer which are stored on the pixel by applying a voltage to the capacitors. Each pixel/capacitor accumulates electrons proportional to the light incident on that pixel. In contrast to CMOS-sensors, where each pixel has a separate charge-to-voltage converter, the CCD-sensor first shifts the signal into the readout register and then converts the charges with only one analog-to-digital converter (AD converter). In order to read out the accumulated charges they get transported in the 'vertical' (vertical as shown in Figure 5.1) direction line by line. This is done by transferring the charges of each pixel to its neighboring pixel. By this, in each shift process the lowest line gets transfered into the horizontal readout register. In

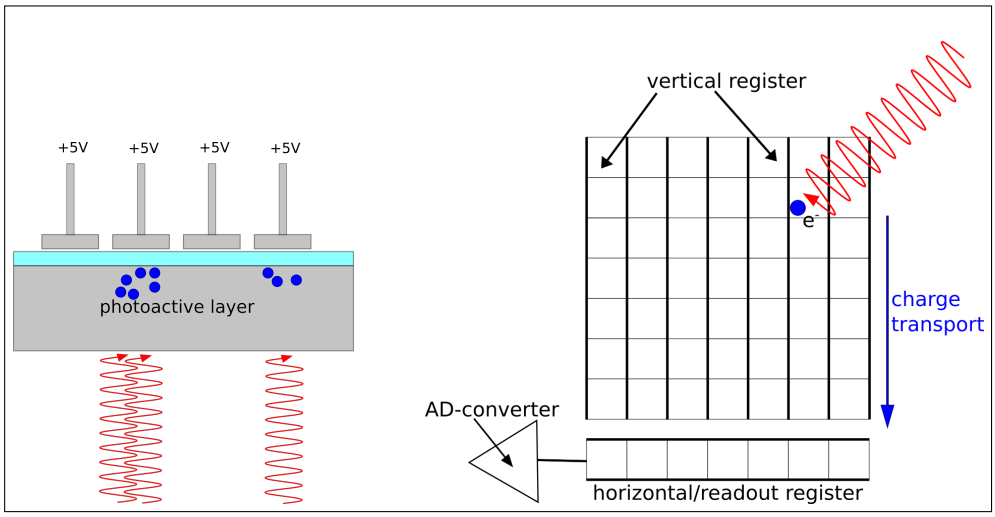

Figure 5.1: The images illustrate the working principle of a CCD-sensor. Impinging photons create photo electrons inside the photoactive layer. During the image acquisition, these electrons are captured on the pixel. To read out the sensor, each row of the sensor gets shifted vertically and is subsequently read out in the horizontal register.

this readout register, the pixels are shifted in the horizontal direction such that the charge on each pixel is first amplified with a charge-amplifier and then converted with an AD-converter into a digital signal.

Electron Multiplying CCDs

Typical CCD cameras have a readout noise of around 5 to 10 electrons per pixel which prohibits the detection of single photons. This readout noise is caused by the AD-converter of the readout register. To overcome the read noise, an EMCCD camera amplifies the signal on each pixel before reading it out with the AD-converter. In doing so, even a single electron on the sensor can be amplified out of the readout noise so that single photons can be detected. However, there are several things that have to be taken into account for the evaluation of the data from an EMCCD camera. In particular the noise that is generated by unwanted charges on the sensor is limiting the performance of an EMCCD camera (see next section). The imaging acquisition of an EMCCD camera works in the same way as for conventional CCD-cameras. Instead of directly converting the charges on the sensor into a digital image, the EMCCD camera features an additional gain register as illustrated in Figure 5.2.

As shown in the image, the shift voltage in the gain register is so high that in each shift process there is a certain probability that an initial charge creates another free

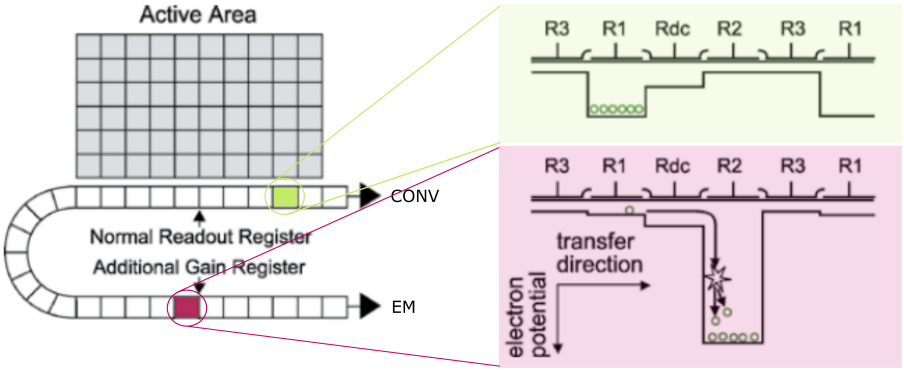

Figure 5.2: The image illustrated the working principle of an CCD sensor both with and without EM-mode. In the conventional mode, the pixels in the readout register are directly converted into a digital signal with the AD-converter. In the EM-mode, the electrons are shifted through an additional gain register where the shift voltage is very high. An initial electron creates an avalanche of electrons which is then read out with an AD-converter. Figure taken and adapted from [39].

charge. The applied shift voltages are on the order of 40 V - 60 V which causes a multiplication per transfer of around $\times 1.01$ to $\times 1.015$. Although this sounds very small, when applied 500 times, a single electron yields around $1.01^{500} = 145$ to $1.015^{500} = 1710$ secondary electrons. The gain can be controlled by adjusting the shift voltage. Hence a single electron on a pixel causes an electron avalanche through the gain register. This amplification process of course only starts if there was at least one initial electron on the pixel. Since each primary electron creates an avalanche of secondary electrons, each event can be amplified out of the readout noise if the gain is sufficiently large.

The amplification of single electrons in the gain register is a statistical process. Consequently, as will be analyzed in section 5.1.2, it is no longer possible to clearly count multiple photons on the same pixel since the output distribution of the gain register for one and two initial electrons overlap. Furthermore also charges on the sensor that were not created by impinging photons (such as thermal charges) get amplified out of the read noise. These background charges cannot be distinguished from electrons that were created by photons coming from the atomic sample. There are different sources of unwanted charges on the sensor which are summarized under the term 'spurious charges'. These are analyzed in the next section.

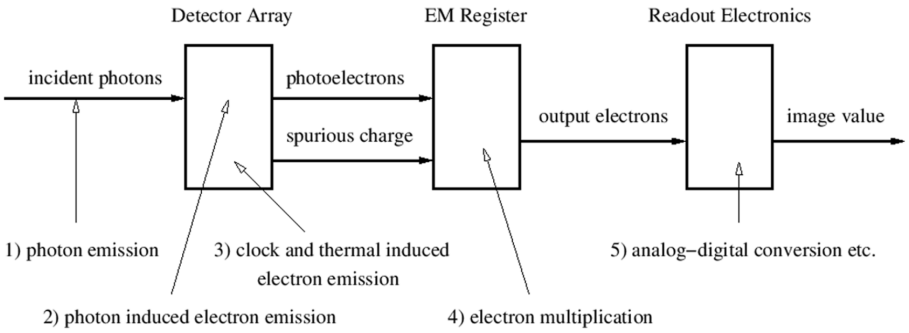

Figure 5.3: The diagram illustrates the different sources of noise and show where they enter the image. The most important sources are the spurious charges that are created on the detector array. Figure taken from [40]

5.1.1 Sources of noise

There are many different noise sources that influence both the output and the performance of an EMCCD camera and that have to be considered when evaluating the data. Figure 5.3 illustrates the different stages in the imaging process where noise can enter the system. The first stage is independent of the camera. The emission from the atomic source is a stochastic processes. The number of detected photons that are collected by the imaging setup is shot-noise broadened and given by a Poisson distribution of mean $\mu = n$ with n being the average number of photons. Also the creation of photoelectrons inside the photoactive region of the camera is a stochastic process which influences the detection efficiency. These two sources only affect the number of detectable photons. The perfomance of the camera is most limited by unwanted charges that are created on the detector array. These charges are not created by photons and are called spurious charges. There are three main contributions to the spurious charges.

- Thermal Charges: In the photoactive region, electrons can be spontaneously excited from the valence band into the conduction band. The bandgap of silicon is $E_G = 1.17\,\mathrm{eV}$. Thermal electrons can be minimized by cooling the sensor to temperatures of around $-70\,^\circ$, which corresponds to a thermal energy of $E_T = k_B T = 0.017\,\mathrm{eV}$ and thus $\frac{E_G}{E_T} = 68.8$.

- Clock-Induced Charges(CICs): These charges are generated during the vertical shift process, i.e. while the charges are shifted across the sensor. In each shift process, there is a small probability that the applied shift voltage creates a free charge. These charges can be minimized by adjusting the readout speed of the camera. There are also new technologies that adapt the waveform of the shift voltage during the readout process which significantly decreases the

amount of clock induced charges [41].

- Dark Counts by Background Light: Background photons, e.g. from the trapping laser or from ambient light sources can also create free charges on the CCD-sensor. Background photons can almost be completely eliminated by encasing the experiment and by using an appropriate filter in front of the camera.

Spurious charges are of course also present in conventional mode but there they disappear in the readout noise. In the EM-mode they are problematic since each electron is amplified by the gain register so that spurious charges cannot be distinguished from charges created by photons from the atomic sample. Especially clock-induced charges are limiting the performance of most EMCCD-cameras since their appearance is more probable than the appearance of charges caused by the other two noise sources.
Another source of noise is the gain register. As explained in the previous section, the electron multiplication is a stochastic process. Hence the output of the gain register cannot be attributed to a definitive number of initial electrons.
The last noise source is the electronics that converts the secondary charges from the gain register into a digital image. This analog-to-digital conversion typically has a noise of a few electrons. This read noise is the limiting noise for conventional CCD-cameras. However, since the gain register produces hundreds of secondary electrons, the read noise is very small compared to the signal and the SNR is very high.
All these noise sources will be characterized for our camera in section 5.2.

5.1.2 Stochastic model for EMCCD cameras

Fig 5.4(a) shows a typical dark image in EM-mode. The image contains a relatively flat background and many bright pixels. The histogram next to it shows the distribution of the output values of the gain register (ADU = Analog/Digital Unit), i.e. the color bar in the left image corresponds to the x-axis of the histogram. Note that the plot is done with a logarithmic y-axis.
The image and the histogram best illustrate the output and hence the working principle of the EM-mode. In the following we imply the easiest description of the output of the EM-mode, that is to separately consider pixels with a charge and pixels without a charge. The pixels in the flat background correspond to pixels with no charge. In the histogram they appear in the peak. If there is no charge on a pixel, the electronics adds an offset to the pixel before converting it into a digital signal. This offset (called baseline) corresponds to the peak position in the histogram at an

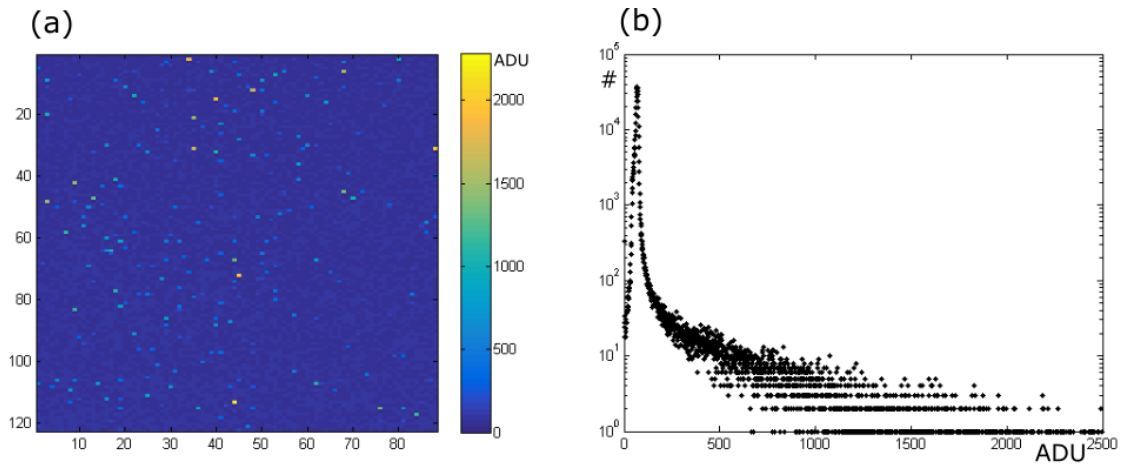

Figure 5.4: (a) shows a typical dark image in EM-mode. It contains a relatively flat background (pixels that do not contain a charge) and many bright pixels (spurious charges). (b) shows a histogram of the pixel values from the image in (a). The histogram is plotted with a logarithmic y-axis. The peak is produced by the pixels without a charge. The tail at high ADUs corresponds to the bright pixels that were amplified before going through the readout electronics.

ADU of around 100. The output of the gain register (before being read out by the AD-converter) can be described by a δ-distribution

$$P_0(x) = \delta(x - b). \tag{5.1}$$

In the readout process, the peak is then broadened due to the electronic noise of typically around $5 - 10\,\mathrm{e}^-$.

The bright pixels of the image correspond to a charge that has been amplified out of the read noise. In the histogram these bright pixels are lying in the tail above the 'no-charge' peak. Since the image was taken with a closed shutter, all the bright pixels here were caused by spurious charges.

If there are n initial charges on a pixel, the output of the gain register can be described by a probability distribution [42] as

$$P_n(x) = \frac{x^{n-1} \exp(-x/g)}{g^n (n-1)!} \tag{5.2}$$

where g is the gain of the amplifier, n the number of primary electrons and x the output/secondary electrons. Figure 5.5(a) shows a plot of the first 3 probability density functions for a typical gain of $g = 500$ on a logarithmic and on a linear scale. For the case of one initial photo electron on a pixel, the output probability function is an exponentially decaying function with a $1/\mathrm{e}$-width of g. These plots

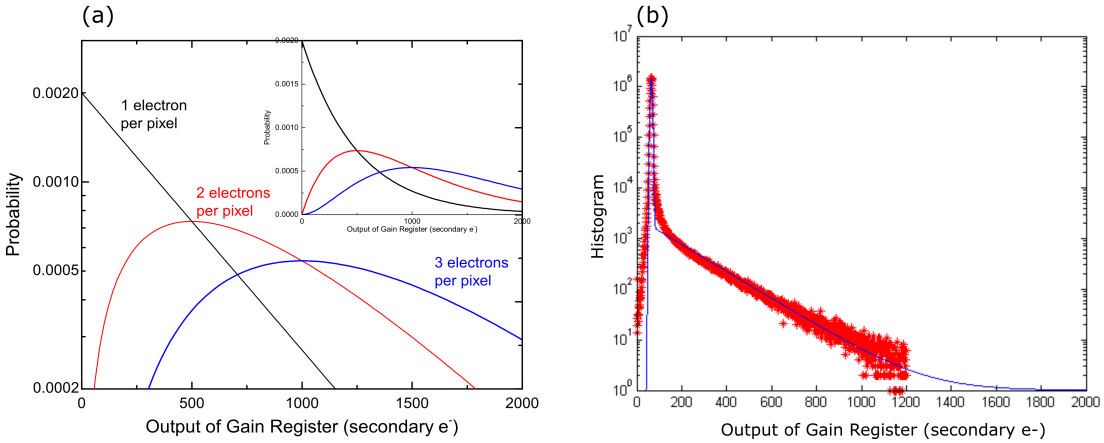

Figure 5.5: (a) shows plots of the output probability functions of the gain register on both a logarithmic and a linear scale. The blot in (b) shows a histogram of the output of the EM-mode and a fit with the function from 5.3. The linear part of the fit in the right plot corresponds to the black plot in the left graph.

illustrate why one can no longer clearly distinguish between one, two or three initial electrons on a pixel. Measuring for example 700 secondary electrons could be caused with almost equal probability from one, two or three initial electrons.

If we are in a regime where there is at most one charge on a pixel as is the case in the histogram from Figure 5.5 and if we assume a gaussian read noise, the easiest model for the output of an EMCCD camera is the convolution of the gaussian read noise with the sum of $P_0(x)$ (for the pixels without a charge) and $P_1(x)$ (for the pixel with one charge).

$$\mathcal{R}(x) = \Big(\mathcal{G}(\sigma_{read}) * \big[p_0\delta + p_1 P_1\big]\Big)(x-b) \tag{5.3}$$

where $\mathcal{G}(\sigma_{read})$ is a Gaussian with a width of the read noise σ_{read}. Figure 5.5 (b) shows a histogram similar to Figure 5.4 but with more data and a fit corresponding to equation 5.3.

With the fit we can determine the read noise as the standard deviation of the Gaussian and the gain from the exponential tail that appears linear in the logarithmic histogram. Although the readout peak and the amplified tail can well be described by the fit, equation 5.3 is not a perfect description of the EMCCD camera. Especially the region right above the read noise is not well described by the fit. There are more sophisticated methods to describe the output of an EMCCD camera as for example [40, 43] which we do not need for our purposes.

From the fit, we can define a threshold above which we will identify a pixel as a

charge. This threshold has to be chosen such that the probability to wrongly identify an empty pixel as one with a charge is small and at the same time the probability for a pixel with a charge to be identified as such to be maximum. For the empty pixels we use the read noise σ_{read} and the baseline b as relevant parameters. If we set the threshold to $3\sigma_{read}$ above the baseline, 0.135% of empty pixels would be wrongly identified as charges. For a threshold of $5\sigma_{read}$, only $2.85 \times 10^{-5}\%$ of empty pixel would be identified as charges. Next we quantify how likely is it that one charge produces an output in the gain register that is above the threshold. For this, we integrate the output probability for one charge $P_1(x)$ from the threshold σ_{th} to infinity. This gives us the probability $\mathscr{D}(\sigma_{th})$ that one initial charge gets amplified above the threshold.

$$\mathscr{D}(\sigma_{th}) = \int_{\sigma_{th}}^{\infty} P_1(x)dx = 1 - \frac{1}{g}\int_0^{\sigma_{th}} e^{-x/g}dx = e^{-\sigma_{th}/g} \tag{5.4}$$

and plot this as a function of the parameter $\xi = \frac{g}{\sigma_{th}}$ in Figure 5.6 for $\frac{\sigma_{th}}{\sigma_{read}} = \{3, 4, 5\}$. This figure shows, that the detection efficiency of an EMCCD camera profits from a higher gain. We will see in section 5.2.2, that we operate our camera in a regime, where the the detection fidelity $\mathscr{D}(\sigma_{th})$ of a charge on a pixel is almost 1.

With this procedure, we can identify the pixels that contain at least one charge but we cannot count multiple charges on a pixel with high fidelity. Hence the performance of an EMCCD camera is best in the regime where there is only one charge per pixel since we can count them with very high fidelity. For this, one wants to spread the signal over as many pixels as possible. However this also increases the number of spurious charges within the region of interest.

Even though, it is not possible to count few photons on the same pixel, it is possible to estimate the number of photons by dividing the output of the gain register by the gain that was determined with the fit of Equation 5.3. Assume, we have n photons on one pixel, then the expected output of the gain register is given by

$$\langle X\rangle_{P_n} = \int_0^{\infty} xP_n(x)dx = (g(n-1)!)^{-1}\int_0^{\infty} x^n exp(-x/g)dx = \frac{g}{(n-1)!}\Gamma(n+1) = ng. \tag{5.5}$$

To quantify the quality of the estimation of the photon number, we need to compute the variance. For the variance we also need the second moment of the output distribution

$$\langle X^2\rangle_{P_n} = \int_0^{\infty} x^2 P_n(x)dx = \frac{g}{(n-1)!}\Gamma(n+1) = (n+1)ng^2. \tag{5.6}$$

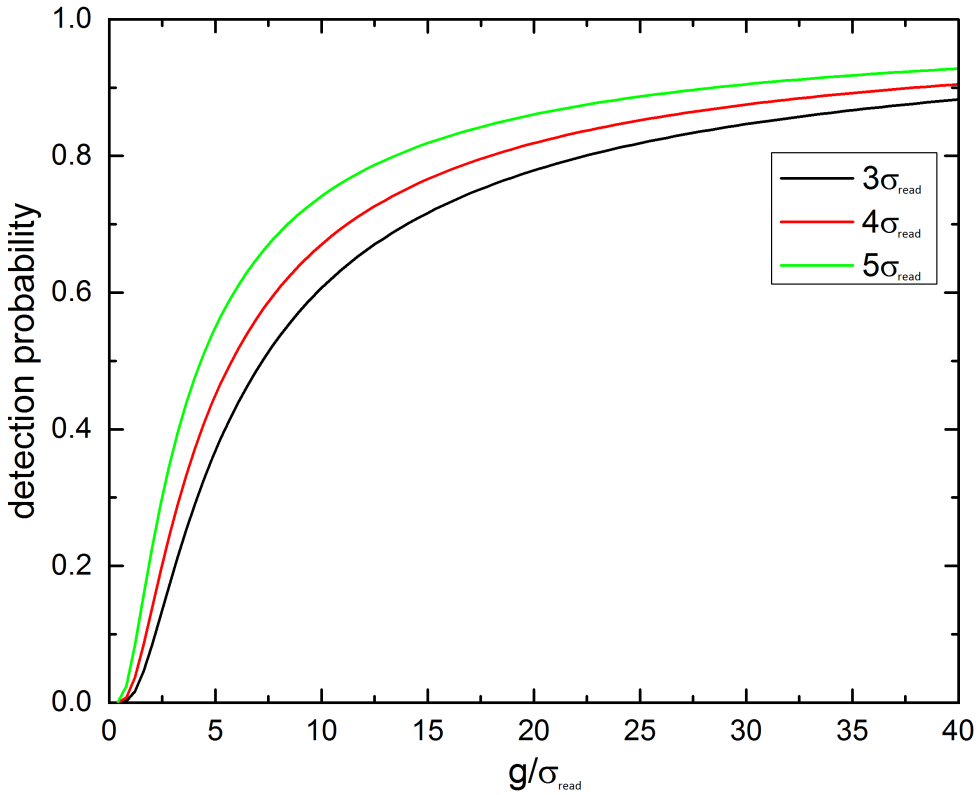

Figure 5.6: The plot shows the detection efficiency of a single charge on a pixel in EM mode for different thresholds. The higher the threshold, the less empty pixels are identified as charges. The higher the gain, the higher is the detection probability of a single charge on a pixel. For very high gains, the detection probability converges towards unity.

Thus the variance can be calculated to be

$$Var(X) = \langle X^2 \rangle_{P_n} - \langle X \rangle_{P_n}^2 = ng^2 \tag{5.7}$$

which gives a coefficient of variation

$$\kappa(X) = \frac{\sqrt{Var(X)}}{\langle X \rangle_{P_n}} = \frac{1}{\sqrt{n}}. \tag{5.8}$$

Hence for many photons the coefficient of variation converges to zero which enables to estimate the number of photons. This estimate becomes more accurate for a high number of photons. This cannot only be applied to the signal on one single pixels, but also to multiple pixels within a ROI.

Active pixels	512×512
Pixel size	$16 \times 16\mu$m
Readout rates	1, 3, 5, 10 MHz
Read noise through EM amplifier[1]	21.7, 32.6, 42.9, 49.2 e^-
Read noise through conv amp (1MHz, 16bit)	8.3 e^-
Quantum Efficiency at 671 nm and $-20\,^\circ$C	$\approx 88\%$
Dark current at $-70\,^\circ$C	0.012 e^-/pix/s
Dark current at $-90\,^\circ$C	0.0035 e^-/pix/s
Amplified Background events[2]	0.005 e^-/pix/s

Table 5.1: The table summarizes the specification of our camera as they are given in the performance booklet.

5.2 Characterization of our detection setup

The EMCCD camera that we use for the detection of few photons is characterized in this section. First we give an overview about camera specifications, then the gain and the different noise sources are characterized.

5.2.1 Specifications of Andor iXon

For the detection of the fluorescence signal of the atoms, we use an ANDOR iXon with a DV887 back illuminated CCD sensor with an AR coated window that has been optimized for 670 nm. The CCD sensor has 512×512 pixels with a pixel size of $16\mu m$. Table 5.1 summarizes the most important specifications of the camera as specified by Andor. Most of the specifications given have been measured by us but do not fully agree with our results. The following sections will present results of the measurements and characterize the gain and noise.

5.2.2 Characterization of the EM-gain

The gain of the camera has been measured as described in section 5.1.2. For the histogram, many dark images were used in order to get good statistics for the exponentially decaying tail. As described in the previous chapter and also shown by Figure 5.6, not only a high gain is important but rather the ratio of gain and readout noise. The gain strongly depends on the temperature. Figure 5.7 shows two graphs of the temperature dependence of the gain. The left graph shows the actual gain

[1] Single Pixel read noise for a preamplifier gain of 5. The values correspond to the different readout rates.

[2] EMgain 1000, 30ms exposure time, $-70\,^\circ$C

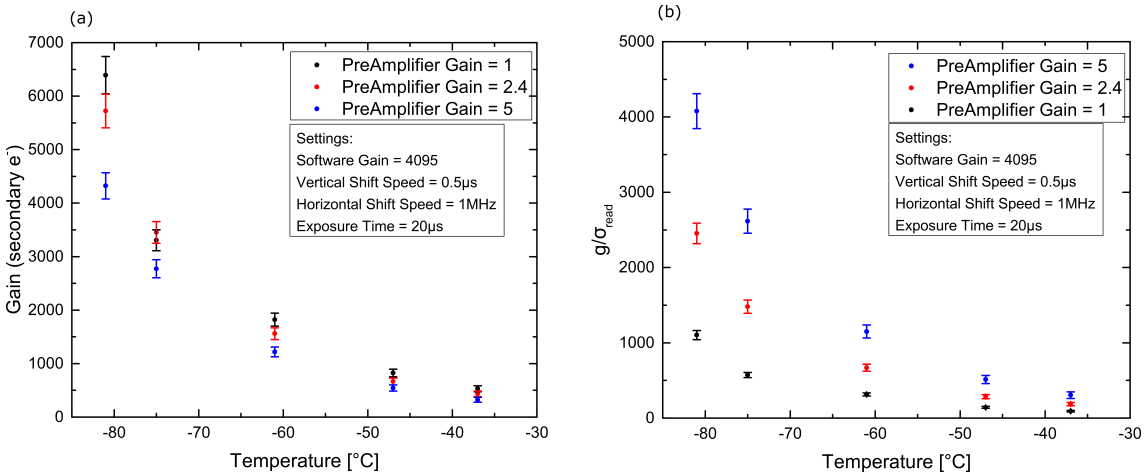

Figure 5.7: The left plot shows the gain as a function of temperature for the three different settings of the pre-amplifier. The right plot shows the same data but rescaled by the read noise. The gain strongly increases with decreasing temperature. For the best gain to read noise-ratio, the highest pre-amplifier gain should be used.

(in output electrons) as a function of the temperature. The right graph shows the parameter $\xi = g/\sigma_{th} \equiv g/(1 \times \sigma_{read})$ also as a function of temperature. The gain increases almost exponentially with decreasing temperature. If one compares the right graph to Figure 5.6, it becomes clear, that the most efficient pre-amplifier gain is a gain of 5 and also that a temperature around $T = -70\,°\mathrm{C}$ provides a sufficiently high gain such that almost all charges can be identified. For a threshold of $\sigma_{th} = 1 \times \sigma_{read}$, we get a $\xi_1 = g/(1 \times \sigma_{read}) \approx 1500$. This corresponds to $\xi_5 = g/(5 \times \sigma_{read}) \approx 300$ when we use a threshold of $\sigma_{th} = 5 \times \sigma_{read}$. Hence, according to Equation 5.4, the detection probability for a single charge is $\mathscr{D}(5\sigma_{read}) = e^{-1/300} = 0.9967$.
In the same measurement also the influence of other settings such as the vertical or the horizontal shift speed on the gain were tested. Except for the temperature and the adjusted software gain, the real gain is almost not influenced by other parameters.

5.2.3 Spurious charges

The most unwanted noise of an EMCCD-camera stems from spurious charges, which are unwanted charges on the sensor that are amplified out of the read out noise. They have been introduced in section 5.1.1. These charges cannot be distinguished from actual photon counts. There are three sources of spurious charges:

1. Thermal Charges

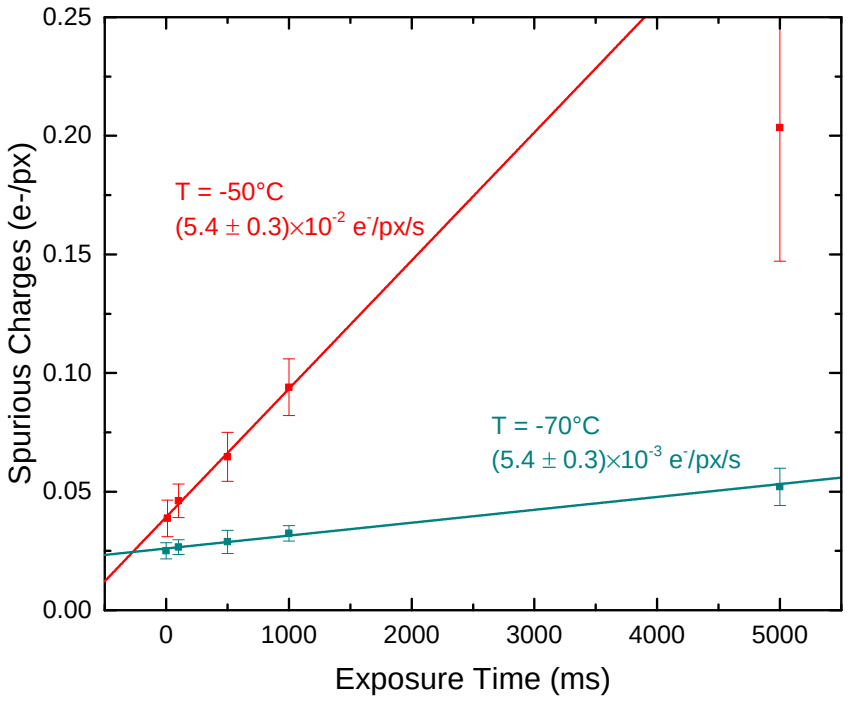

Figure 5.8: The graph above shows shows the increase of thermal charges for longer exposure times. From this increase, we can estimate the generation rate of thermally excited charges on the sensor. This was done for temperatures of $T = -50\,°\mathrm{C}$ (red) and $T = -70\,°\mathrm{C}$ (green). The last point of the red data points is already in the regime where it is very likely to have more than one charge on a pixel. Due to our evaluation method, we underestimate the number of charges for this case. Hence this point is neglected for the linear fit.

2. Clock-Induced Charges

3. Dark Counts by Background Light

In this section all three sources are measured and (if they exist) compared to the specifications from Andor.

Thermal charges

Thermally excited charges are expected to be negligible since the sensor is cooled down to temperatures around $-70\,°\mathrm{C}$. In order to quantify them, we analyze the increase of charges with increasing exposure time with closed shutter. The increase for longer exposure times is only caused by thermal charges since the generation of CICs is only caused by the shift process which is the same for all exposure times. Since we are dealing with a very low number of charges, the images are taken in EM-mode and then converted into binary images. By counting the number of photons

on the images for different exposure time, the generation rate of thermally excited charges can be deduced. Figure 5.8 shows the data for two different temperatures. The red data points were measured at a temperature of $-50\,^{\circ}\mathrm{C}$ and the green data points where measured at $-70\,^{\circ}\mathrm{C}$. As expected, the thermally excited charges increase linearly in time. For very long times, one enters the regime, where it becomes likely that one pixel carries more than one electron which are not correctly identified by the method of converting the image into a binary image. However, we can fit a linear function to the data points below 1 s to deduce the rate of generation for thermal electrons. We find for the two different temperature

$$\begin{aligned} \mathcal{T}_{-50} &= (5.4 \pm 0.3) \times 10^{-2} \mathrm{e}^-/\mathrm{px/s} \\ \mathcal{T}_{-70} &= (5.4 \pm 0.4) \times 10^{-3} \mathrm{e}^-/\mathrm{px/s} \end{aligned} \tag{5.9}$$

The measured value for a temperature of $-70\,^{\circ}\mathrm{C}$ is even lower than the specifications that are given by Andor of $\mathcal{T}_{-70}^{Spec} = (1.2) \times 10^{-2} \mathrm{e}^-/\mathrm{px/s}$. In the experiment we typically image for around $40\,\mu$s which corresponds to 2.2×10^{-7} thermal electrons per pixel.

Clock-induced charges

Clock-induced charges (CIC) are unwanted charges that are created during the shift process and can be considered as the detection limit of EMCCD-cameras. They also occur in normal CCDs but are typically so low that they disappear in the read noise. CIC can be minimized by configuring both the clock rate and the clock form of the readout [41]. In the case of the Andor iXon only the vertical shift speed[3] (VSS) can be adjusted. The vertical shift speed is the time, the shift voltage is applied between the pixels. The longer the shift voltage is applied to the pixels, the more probable it is that a free charge is created. However if the shift voltage is applied for a too short moment, the charges are not properly transported over the sensor. One expects the amount of CIC to increase with both the VSS and with the distance from the readout register. The more often the pixels have to be shifted, the more probable it gets to create a charge. Hence the number of CICs should increase with increasing distance from the readout register.
In order to determine the amount of clock-induced charges, the sensor is cooled down to $-74\,^{\circ}\mathrm{C}$ and the shutter is closed. The exposure time is set to $40\,\mu$s so that

[3] Although the parameter is called shift speed, it indicates the time, the shift voltage is applied. The speed with which the charges are transported is determined by the horizontal shift speed which is kept constant in the evaluation of the CICs.

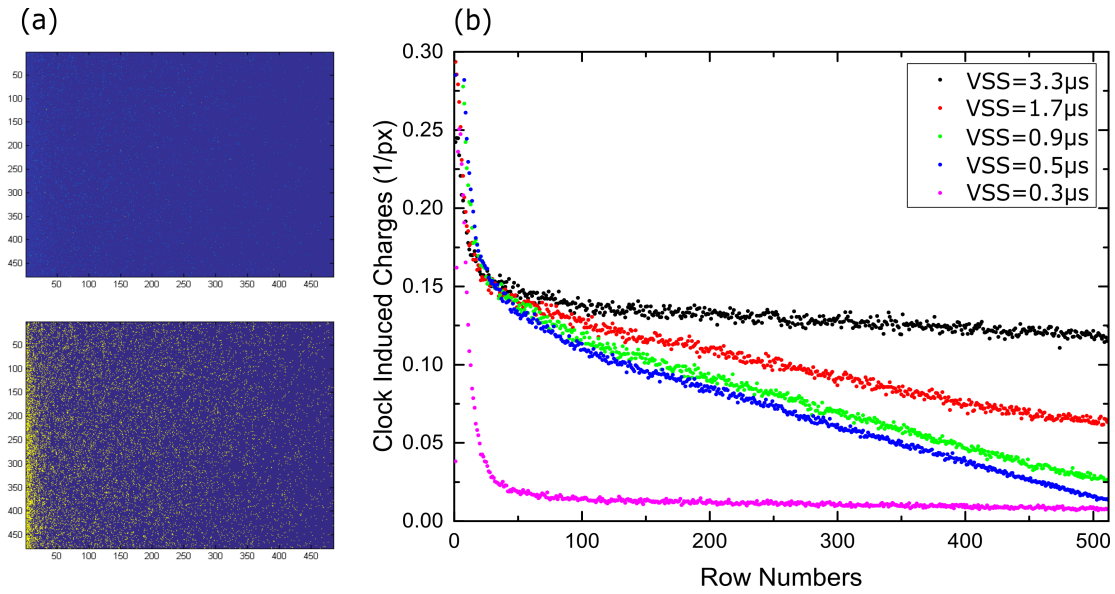

Figure 5.9: The image on the upper left side is a raw image, taken with shutter closed. This image is converted into a binary image, which is shown below. In these images one can already see an increase in noise from right to left. The plot on the right side shows the averaged percentage of CICs per column for all different shift speeds.

both dark electrons and electrons created by background light do not influence the measurement. The camera settings were set to

1. Horizontal Shift Speed = 1 MHz
2. Software Gain = 4090
3. Pre Amplifier Gain = 5
4. Temperature = −74 °C
5. Actual Gain ≈ 2870 e^-

For each value of the VSS, around 70 images are taken and then converted into binary images as described in Section 5.1.2 with a threshold of $5\,\sigma_{\text{read}}$. All events can be attributed to CICs. For each image, the CICs in each column are counted and averaged over all 70 images. Figure 5.9(a) shows a typical dark image both in raw and binary format and the plot in (b) the average number of clock induced charges in each column of the 512×512 pixel image for all possible shift speeds. The sensor is read out on the right side of the image, so that the charges get shifted to the right. As already explained, the CICs are produced during the shift process. As expected, the amount of CICs increases with increasing distance from the readout register and decreases with decreasing VSS. The lowest amount of CIC is reached with a VSS of 0.3 µs and amounts to approximately 0.007 CIC/px which

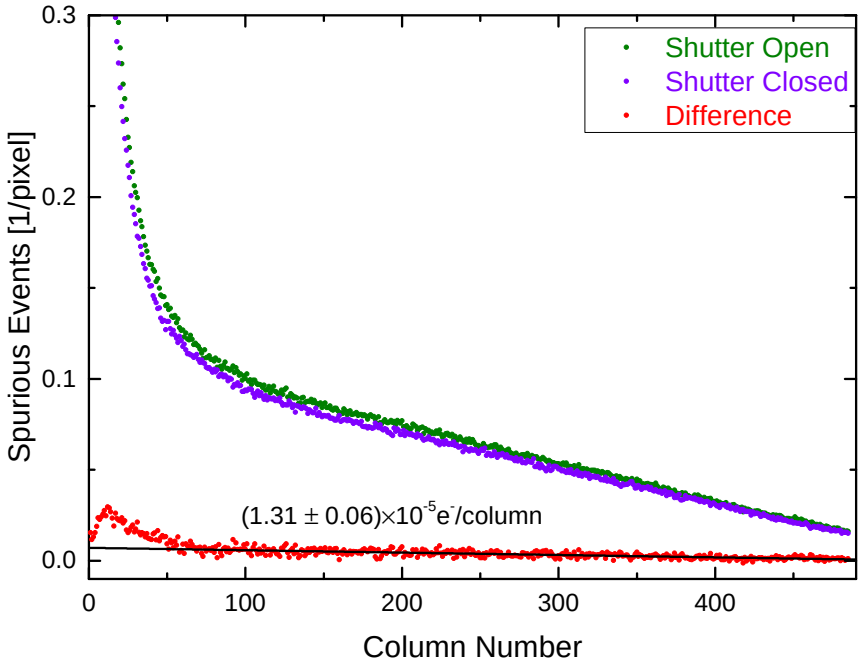

Figure 5.10: The plot shows the averaged events per column with an open shutter and with a closed shutter. The difference of them is also plotted which enables to determine the charges that are produced by background photons.

is comparable to the specifications given by Andor of 0.005 CIC/px. Unfortunately when using a VSS of 0.3 μs all the charges from the signal on the sensor get lost so that this mode is not usable. Hence the lowest achievable value for CICs is reached for a VSS of 0.5 μs on the right side of the sensor. Like this we can reach a value of around 0.02 CIC/px which is much higher than the specifications. This will impair the detection fidelity of single atoms since it increases the lower threshold for identifying an atom.

Dark counts by background light

Dark counts that are caused by ambient background light can almost be completely eliminated by encasing the experiment and covering all light sources within the range of the camera. Furthermore a one inch SM-tube with a band pass filter (Semrock FF01-675/67-25) is used in order to further block stray light and to filter out the 1064 nm light from the trapping beams. In order to quantify the background events, we can compare images with an open shutter to those with a closed shutter. For this measurement, a typical experimental sequence was used but no atoms were prepared. Hence we can analyze all the spurious light that impinges on the sensor. Due

to the low photon number, the evaluation of the images is done exactly like in the measurement for characterizing the CICs. Hence, the difference in charges is caused by the ambient light. Again one expects a slight increase of charges with increasing distance from the read out register since photons can still create charges during the readout. Figure 5.10 shows a plot of the average number of events in each column of the sensor. This plot was generated in the same way as the plots in Figure 5.9 but it shows data with both open shutter (green) and closed shutter (purple). The purple data points in the graph can be allocated to CICs. The green data points are the averaged events for an open shutter. The plot also shows the difference between the purple and green data points in red. This difference in counts can be allocated to background photons. The images were taken with an exposure time of 40 μs which is a typical value for the imaging sequence. A linear fit to the linear part of the red data points gives a slope of $(-1.308 \pm 0.06) \times 10^{-5}$ events/column. These images were read out with a horizontal shift speed of 1 MHz so that one shifted column corresponds to a time interval of 1 μs, thus giving $(-1.308 \pm 0.06) \times 10^{-5}\,\mathrm{events/(px \times \mu s)}$. For an image with an exposure time of 40 μs and a ROI at a distance of around 20 lines from the read out register, this corresponds to approximately $7.8 \times 10^{-5}\,\mathrm{e^-/px}$.

For a typical image with an exposure time of 40 μs at a temperature of $T = -70\,^\circ\mathrm{C}$, we collect

$$\begin{aligned} n_{CIC} &= 0.02\,\mathrm{e^-/px} \\ n_{BG} &= 7.8 \times 10^{-5}\,\mathrm{e^-/px} \\ n_{thermal} &= 2.2 \times 10^{-7}\,\mathrm{e^-/px} \end{aligned} \tag{5.10}$$

This show, that the performance of the camera is limited by CICs. Hence we neglect the other two noise sources. To identify a single atom, its signal has to overcome the noise from CICs. The signal of the atom is distributed over several pixels, which we call the region of interest (ROI). The probability to find n CICs in a ROI with N pixels is given by

$$P_{\text{n events}} = \binom{N}{n} (1-p)^{n-N} p^n. \tag{5.11}$$

The graph in Figure 5.11 shows these probabilities for $n = 0, 1, 2, 3$ as a function of the size of the ROI with a probability of $p = 0.02$. Within a typical ROI with 10 pixels, there are at most 2 CICs. Hence, we need to detect around 10 photons per

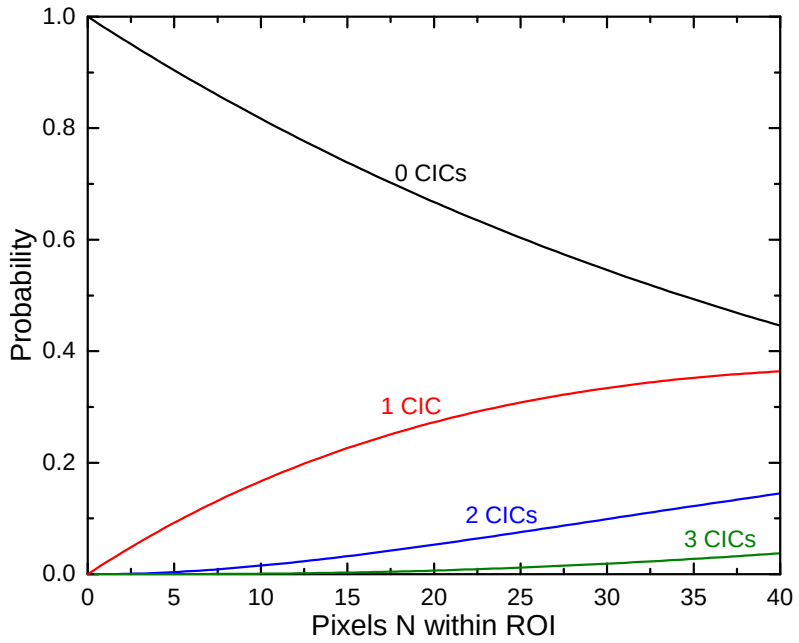

Figure 5.11: The graph shows the probability to find $n = 0, 1, 2, 3$ CICs within the ROI as a function of the size of the ROI for a probability of $p = 0.02$. For small ROI, there are at most 2 CICs within the ROI. This sets a threshold for the detection of single photons.

atoms within the ROI to identify an atom. The next chapter shows that we collect enough photons to identify single atoms.

Technical correction

We found that the noise gradient in the images as shown for example in Figure 5.9 is not primarily caused by the longer read out of pixels that are far away from the gain register. When we record images with LabView, the cleaning cycle of the camera always runs with a speed of around $3\,\mu$s/line and is not adjusted to the chosen vertical shift speed as is done when e.g. using the Andor software Solis. Hence the cleaning cycle itself produces a high amount of CICs. Pixels close to the readout register have been shifted over the whole CCD-chip by the cleaning cycle and thus contain a lot of spurious charges. The further away a pixel is from the readout register, the less CICs have been produced by the cleaning cycle since after the image acquisition the pixels get shifted with a different VSS. This explains, why all VSS give the same amount of CIC on the left side in Figure 5.9 and why the offset of the different VSS settings is not the same. Hence the image is read out to the left and the amount of CICs that is produced by the shift process can be deduced from the offset on the right site in the graph in Figure 5.9. We do not know

yet whether it is possible to adjust the cleaning cycle in LabView, but this would decrease the spurious noise in our images.

6 Single Atom Detection

After we have gained a good understanding of the working principle of the EMCCD-camera and on the dipole transitions of ^{6}Li , we can apply this knowledge to image and identify a single atom. Only state $|3\rangle$ has a completely closed optical transition, so we will analyze only data from this state here. For this we prepare a single atom in state $|3\rangle$ in the ground state of our microtrap.

For the preparation of this atom we start by preparing two atoms in states $|1\rangle$ and $|2\rangle$ in the ground state of the microtrap as explained in Chapter 3. We remove the atom in state $|1\rangle$ by ramping the magnetic offset field to 27 G where the magnetic moment of state $|2\rangle$ vanishes. By applying a magnetic field gradient at this offset field and lowering the depth of the potential well, we only spill state $|1\rangle$, while the atom in state $|2\rangle$ remains in the trap.

We then drive a passage from state $|2\rangle$ into $|3\rangle$. For this we apply a RF-pulse that we sweep over the resonance frequency of the bare transition from $|2\rangle$ to $|3\rangle$. By slowly sweeping the frequency of the RF-pulse across the resonance frequency, we can adiabatically transfer the atom from $|2\rangle$ to $|3\rangle$.

We can check the preparation fidelity for a single atom by loading it into the micro-MOT and by counting the atom number. The preparation and the detection of 2 atoms with the microMOT was done with $97 \pm 1\,\%$. This sets a lower bound to the detection fidelity of a single atom with the microMOT. The preparation of an atom

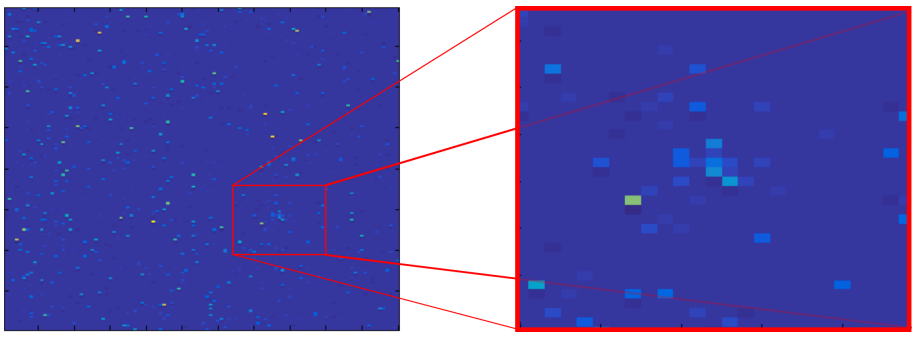

Figure 6.1: The noisy background of the raw images in the EM-mode make the identification of single atoms difficult. We therefore have to develop an evaluation method that can identify single atoms with very high fidelity.

in state $|2\rangle$ was done with a fidelity of around 95 %. Due to technical difficulties in the experiment, the transfer from $|2\rangle$ to $|3\rangle$ could only be realized with a fidelity of around 90 % so that the preparation fidelity for an atom in state $|3\rangle$ is only on the order of 85 ± 5 %.
We now apply our new imaging technique by illuminating the single atom in state $|3\rangle$ with pulses of resonant laser light as explained in Chapter 4 and capture the fluorescence signal on the EMCCD-camera. Figure 6.1 shows a raw image taken in EM-mode with an imaging time of 11 μs of one atom in state 3. Due to the noisy background it is often impossible to tell whether there was an atom by just looking at the images. Hence we need a reliable evaluation method that identifies single atoms. This chapter will apply the things that have been learned about the EM-mode of the camera and present the development of different methods to extract as many information from the data as possible.

6.1 Identification of single atoms

In order to test different evaluation methods, we always use the same set of data and compare the outcomes. This set contains around 700 images. One half of these images (called part $\mathscr{P}_1$) was taken after having prepared one atom in state $|3\rangle$. The other half had no atoms prepared (called part $\mathscr{P}_0$). As explained above, the preparation fidelity of an atom in state $|3\rangle$ was only on the order of 85 ± 5 % so that part $\mathscr{P}_1$ also contains images without atoms. The atom was imaged for 11 μs and the trap was switched off for the imaging procedure.
Due to the finite preparation fidelity, even for a perfect detection fidelity, we should only identify 85 % of the images from $\mathscr{P}_1$ as an atom. We can use this to estimate the detection fidelity of our setup. The probability P_{tot} to detect an atom in $\mathscr{P}_1$ is given by

$$P_{tot} = p_{prep} \times p_{detect} = 0.85 \times p_{detect}. \tag{6.1}$$

Hence the detection fidelity of the setup can be estimated by

$$p_{detect} = P_{tot}/p_{prep} = P_{tot}/0.85. \tag{6.2}$$

Without any knowledge of the EM-mode of the camera, one would most likely choose a rectangular region of interest (ROI) around the signal of the atoms and directly

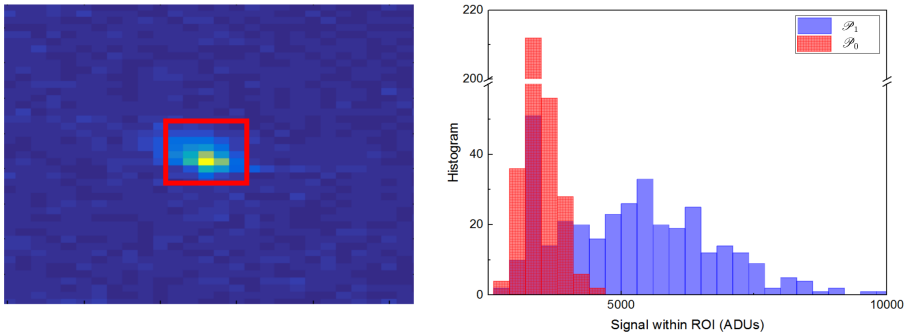

Figure 6.2: The image is the average of all images and is used to chose the ROI. The histogram shows the sum of the counts within the ROI for each image from $\mathscr{P}_1$ and $\mathscr{P}_0$. The overlap between the two data sets is very large such that it is impossible to detect a single atom with high fidelity.

sum up the counts of the camera within this ROI. To choose this ROI we average all images to see how the signal is distributed on the chip of the camera.
Figure 6.2 shows the averaged image with an example for a rectangular ROI. In the histogram next to it, the raw counts within the ROI are summed up for both data sets $\mathscr{P}_0$ (red) and $\mathscr{P}_1$ (blue). The red and the blue data overlap very much such that the identification of a single atom on a single image cannot be done with a high fidelity. Hence we need a more sophisticated evaluation method.

Obviously the method above fails due to two reasons. On the one hand the ROI is too large such that it contains a high number of pixels without signal. Second, these pixels contribute with the read noise and spurious charges to the signal. To improve this method we need to define an improved ROI and to get rid of the read noise of the empty pixels.
In the first approach we will try to choose an optimized ROI and to eliminate the read noise of the background pixels by applying the things that we have learned about the EMCCD-mode. However, this method cannot get around spurious charges in the ROI which will limit the detection fidelity of a single atom. In the second approach we try to only sum up the pixels that contained signal from the atoms by searching for clustered bright pixels in the processed images.

6.1.1 Counting (binary) events within an optimized region of interest

In order to achieve the best signal-to-noise ratio, the ROI has to be as small as possible but contain as much signal as possible. For this, again all images are

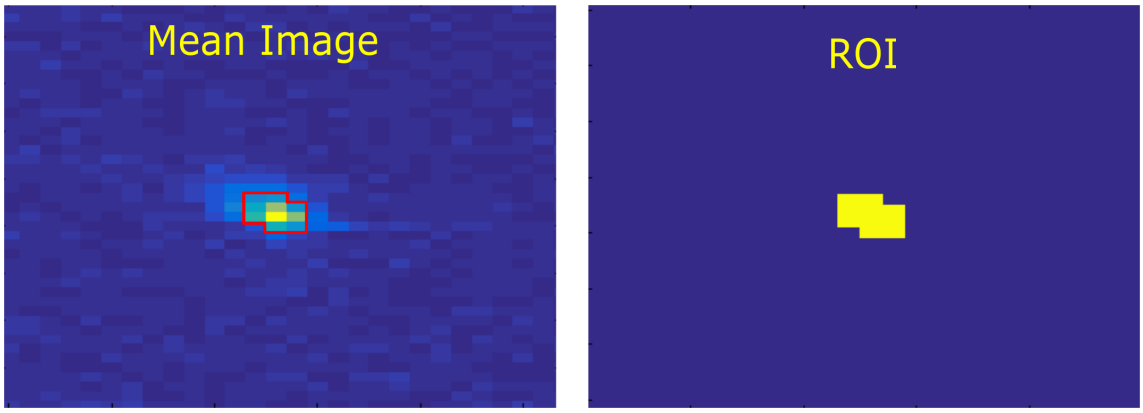

Figure 6.3: The first image is the mean image of all images from $\mathscr{P}_1$. With a threshold of $I_{th} = 0.2I_{max}$, we get a ROI with 10 pixels. The ROI is shown in the second image. With this method, we can select a only the pixels that contain a lot of signal.

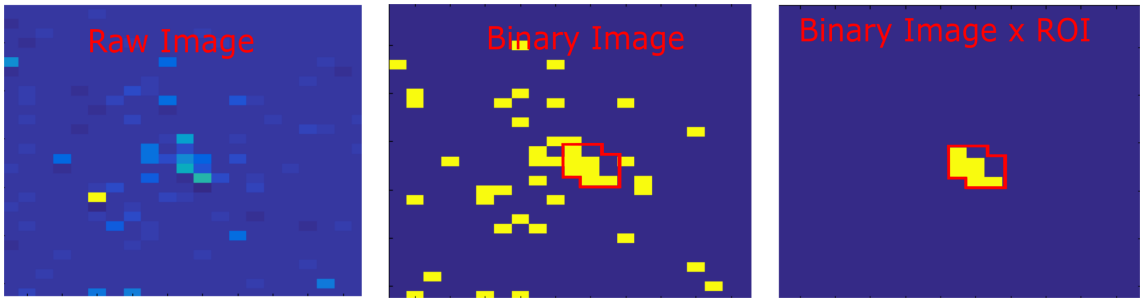

Figure 6.4: By converting the raw image into a binary image, we can eliminate the read noise. Each pixel below the threshold is set to zero so that they do not contribute to the signal. All pixels above the threshold contain at least one charge so that we set them to 1.

averaged but instead of choosing a rectangle around the signal, the ROI is chosen such that it contains all pixels with a signal above a certain threshold. Figure 6.3 illustrates this procedure. The first image is the mean of all images from $\mathscr{P}_1$. With a threshold of $I_{th} = 0.2I_{max}$ we get a ROI with 10 pixels. For the evaluation of the data, we will only sum up the pixels within this ROI. With this method we only choose the pixels that collect the most signal.

Once the ROI is chosen, we apply the knowledge that we gained by analyzing the EM-mode of the camera. As explained in Chapter 5, we can define a threshold above which we identify a pixel as a charge. We chose a threshold of $\sigma_{th} = 5 \times \sigma_{read}$. All pixels with less counts than the threshold did not contain a charge. Hence we set each empty pixel to zero and each pixel above the threshold to 1.

Figure 6.4 shows an example of a raw image that is converted with this method into a binary image. In the binary image, each yellow pixel contained at least one charge

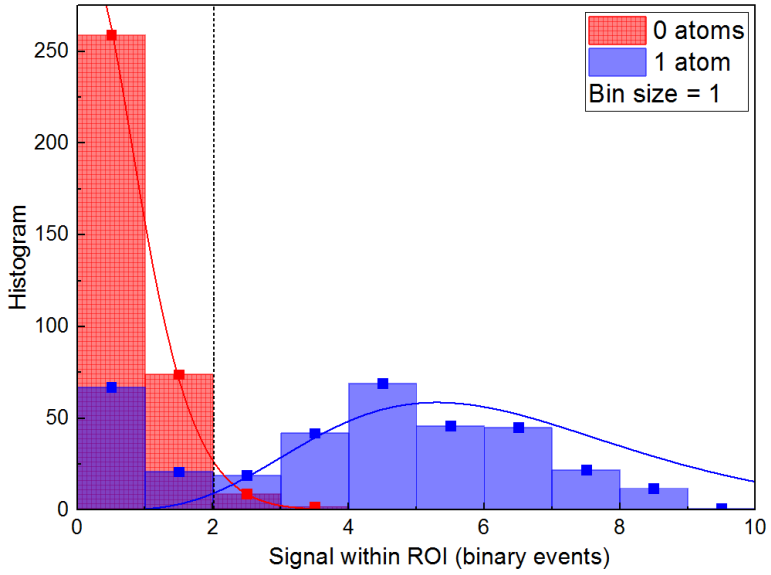

Figure 6.5: The histogram shows the data that was obtained by first converting the images into binary images and then summing up the events within the optimized ROI. The red data was fitted wit Equation 5.11 and yielded a probability for spurious charges of $p = 0.024 \pm 0.003\,\mathrm{e}^-/\mathrm{px}$. This agrees with the values that have been measured in Chapter 5. The blue graph is a Poisson distribution with mean $\mu = 5.3$ which does not describe the data very well.

and the blue pixels did not contain any. The chosen ROI is marked in red. For the last image, all pixels outside the ROI were set to zero. With this method the single images are processed and the events within the ROI are summed up. Figure 6.5 shows a histogram of the sum within the ROI. Again the red data corresponds to $\mathscr{P}_0$ and the blue data to $\mathscr{P}_1$.

Let us first compare the red data to the characterization of the spurious charges from Chapter 5.2. For this we fit the data with Equation 5.11 with $N = 10$. The fit yields a result of $p = 0.024 \pm 0.003\,\mathrm{e}^-/\mathrm{px}$. In the experiment, the signal of the atoms was shifted to column 450 of the CCD-chip and imaged with a VSS of $0.5\,\mu\mathrm{s}$. As was explained in Chapter 5 and shown in Figure 5.9, this number of spurious charges agrees very well with the expected value.

This advantage of this evaluation method is that it sets a clear threshold that has to be overcome to identify an atom. For the case that there was no atom prepared, the probability to count more than one bright pixel in the ROI is only $P_1 = 2.4\%$ and to count more than 2 is only $P_2 = 0.16\%$. With a smaller ROI P_1 and P_2 can be even further decreased.

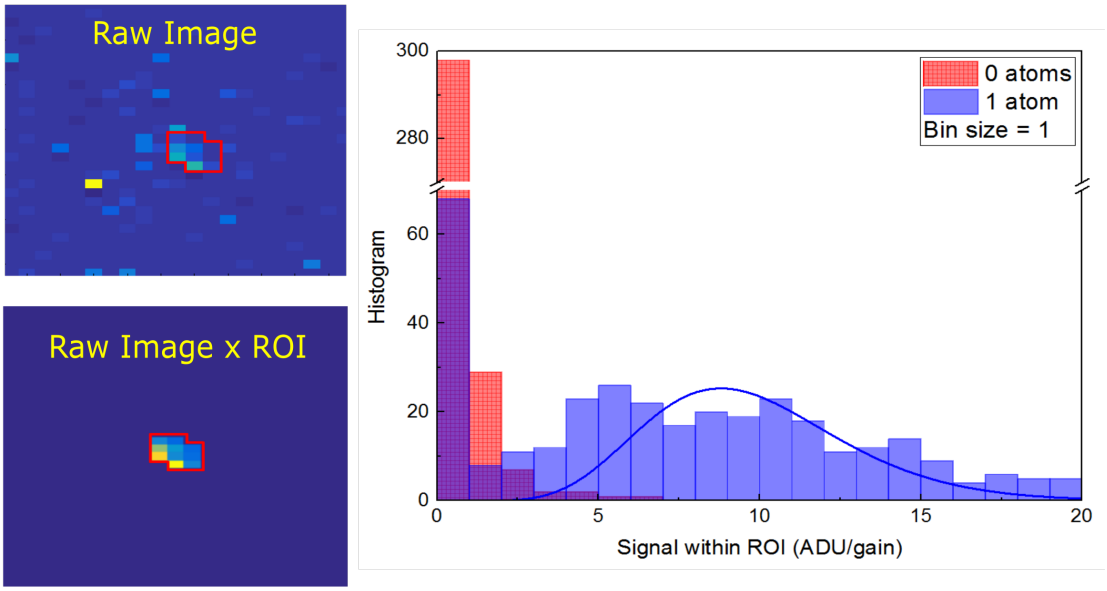

Figure 6.6: For the data in the histogram, the raw counts within the ROI were summed. By dividing by the gain of the EM-register, we can estimate the number of photons. However in this method, it is hard to find a threshold for the identification of single atoms.

The number of photons of $\mathscr{P}_1$ that are counted within the ROI should be well described by a Poisson distribution. Hence we can try to fit such a distribution to the blue data. As can be seen in the histogram, the data is not well described by a Poisson distribution. The reason for this is that the method underestimates high photon numbers. When there are e.g. 10 photons within a ROI of 10 pixels, the probability that they are distributed over all pixels is very small. Hence there are typically several pixels that contain more than one charge which we so far counted as one.

To account for pixels with more than one charge, we can try to estimate the real number of photons as described in section 5.1.2. For this we sum up the raw counts on the bright pixels and divide the output by the gain. The images are processed in the same way as above but instead of setting each pixel above the threshold to 1, we keep the pixel value from the raw image. For many photons, this gives a more accurate estimation of the photon number. Figure 6.6 illustrates this method and shows the histogram. The x-axis corresponds to the estimate of the photon number. The blue line is a Poisson distribution with a mean of $\mu = 9.3$. This graph describes the data of higher photon number quite nicely. However with this method it is hard to define a threshold to identify single atoms since the estimation of the

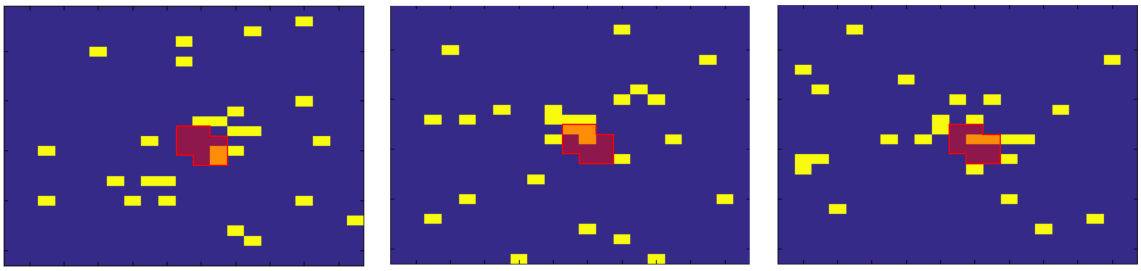

Figure 6.7: The three images show cases where an atom might have been prepared but there was not enough signal within the ROI to identify it.

photon number becomes imprecise for a low number of photons which causes the distributions from $\mathscr{P}_0$ and $\mathscr{P}_1$ to overlap in the histogram in Figure 6.6.

These methods already allow to identify single atoms with a good fidelity. This fidelity even increases for longer imaging times. However as one can already guess from the second picture in Figure 6.4, the fixed ROI does not always capture all photons. Furthermore, the number of events below the threshold (in Figure 6.5) is on the order of almost 30 % which does not agree with the expected preparation fidelity of 85 %. Taking a closer look at the single images shows that in some cases there was an atom but the signal was not focused into the ROI. The three images in Figure 6.7 illustrate three examples where there might have been an atom but it was not detected. To improve the detection fidelity we keep the trapping potential on during the imaging procedure to better localize the fluorescence signal of the atom.

6.1.2 Pinning the atoms to their initial position

Figure 6.7 shows three example images where an atom might have been prepared but not identified due to a wrong position of the ROI. In order to better localize the atoms, we tried keep the trapping potential on during imaging and even ramping it a little bit deeper.
For this we repeated the measurement from above with exactly the same experimental parameters but we ramped the trap to 10 mW which corresponds to a trap depth of 27 E_{rec} in the excited state.
Figure 6.8 shows two histograms that were obtained with the two methods above. They look almost similar to the histograms from Figures 6.5 and 6.6 which we expect since the average photon number should be exactly identical. However, the number of events below a threshold is lower than it is in the case where we switched off the trap.
If we set the threshold for identifying an atom to $N = 2$ for the binary histogram,

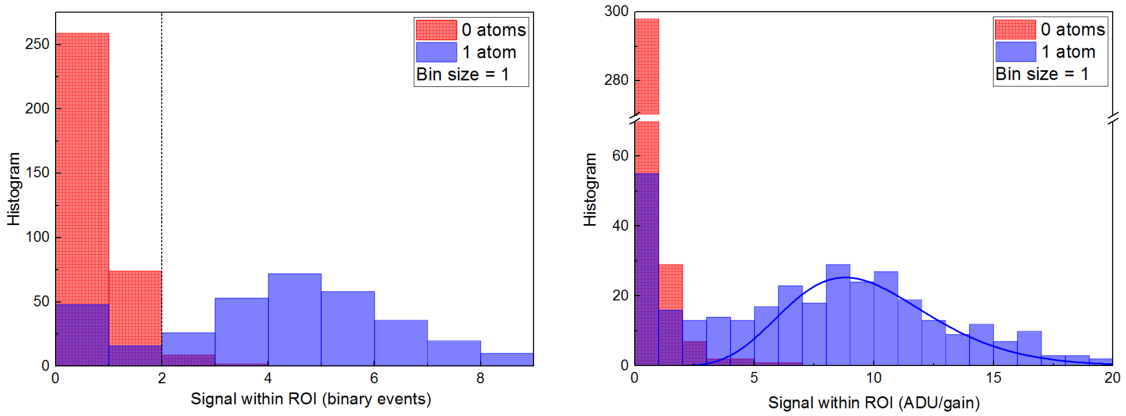

Figure 6.8: The two histograms present the data that was taken when we ramped the trapping potential to around $27\,\mathrm{E_{rec}}$. The left histogram shows the data when the images are converted into a binary image. The right histogram shows the second evaluation, where the number of photons is estimated. When we keep the trap on during imaging, the number of detected atoms is always higher than in the case where the trap is switched off.

we get with our dataset

$$\begin{aligned} N_{1atom}/N_{tot} = &\quad 74\,\% \quad \text{Without Trapping Potential} \\ N_{1atom}/N_{tot} = &\quad 82\,\% \quad \text{With Trapping Potential} \end{aligned} \tag{6.3}$$

With equation 6.2 we can estimate the detection fidelity

$$\begin{aligned} p_{detect} = &\quad 87 \pm 4\,\% \quad \text{Without Trapping Potential} \\ p_{detect} = &\quad 96 \pm 5\,\% \quad \text{With Trapping Potential} \end{aligned} \tag{6.4}$$

if we assume an error of 5 % on the preparation fidelity.
Also in other runs we saw, that the number of detected atoms is always higher when the trapping potential is kept on during imaging. Furthermore the number of detected atoms for this method always almost agrees with the preparation fidelity that we measured with our other imaging setup.

Also when the trapping potential is kept on during imaging, a fixed ROI always has the disadvantage that it contains empty pixels: Especially when no atom was prepared it contains spurious charges that set a relatively high threshold. To further

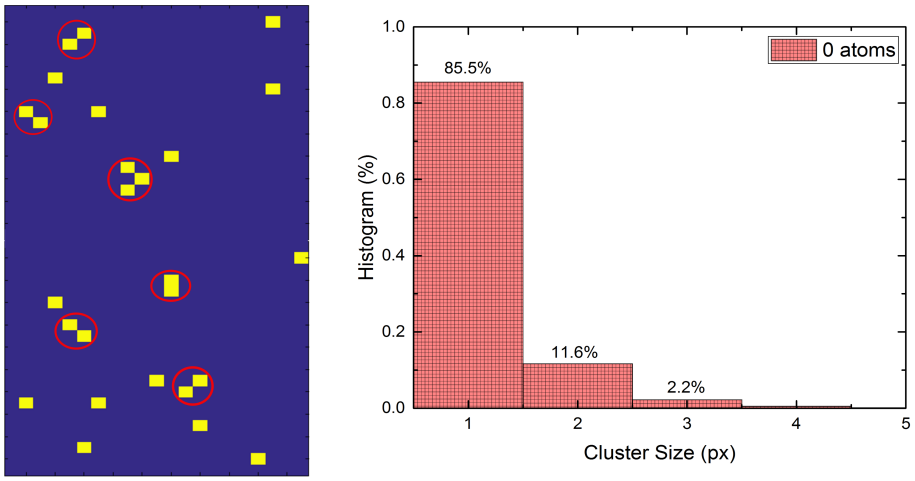

Figure 6.9: Spurious charges are randomly distributed over the CCD-camera. Hence the probability to find connected bright pixels is very low. With MatLAB we can locate these clusters. The histogram on the right side shows that bright pixels appear alone in 85.5%. Is is very unlikely to find clusters with more than 3 pixels.

improve the ROI there is another approach. Instead of fixing a ROI for each image, we search for clusters in the binary images. This approach is explained in the next section.

6.1.3 Searching for clustered bright pixels

Another method to evaluate the images is to look for clustered bright pixels. For this, the image is first converted into a binary image as explained in the previous section. If there are only spurious charges on the sensor, it is very unlikely to find large clusters of bright pixels. Instead, there should only be clusters of 2-4 bright pixels.

This evaluation method more effective for longer imaging times where the signal of the atoms is spread over many pixels. Hence here we analyze data that was imaged for 23 μs. The remaining parameters were the same as for the data in the previous section.

As a reference we start to analyze images without atoms, i.e. data set $\mathscr{P}_0$. Figure 6.9 shows an example of a binary image without an atom. All clusters of bright pixels are identified with MatLAB. As illustrated in the figure, both direct and diagonal neighbors are taken into account.

The data of $\mathscr{P}_0$ gives us again a threshold that needs to be overcome by the data from $\mathscr{P}_1$. For this we characterize the clusters in empty images with a histogram. The normalized histogram is also shown in Figure 6.9. The histogram shows that

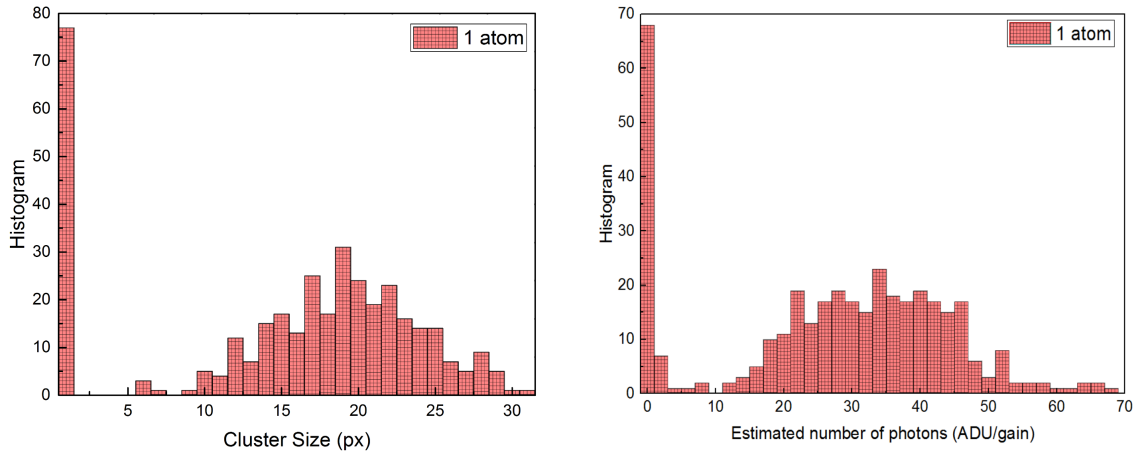

Figure 6.10: Neglecting all clusters with a cluster size below 5, we sum up the number of bright pixels in the processed images. The left histogram shows the size of the clusters. By summing up the raw counts of these clusters and dividing the outcome by the gain, we can estimate the number of photons in the same way as was explained in the previous section. This is shown in the right histogram.

most of the bright pixels (85.5 %) are not clustered and appear alone. Furthermore it is very unlikely to have clusters with more than 3 pixels and that there is never a cluster with more than 5 bright pixels.

To ensure that we only sum up signal that is coming from an atom, we use a threshold of 5 pixels for $\mathscr{P}_1$. All clusters below that size are neglected and all clusters with 5 or more pixels are attributed to an atom. Figure 6.10 shows a histogram of the cluster size of $\mathscr{P}_1$. We cannot directly compare this evaluation method to the method described in the previous section since we used a different set of images. However by counting the number of images that produce a signal above the threshold, we get

$$N_{1atom}/N_{tot} = 79\%, \tag{6.5}$$

which corresponds to a detection fidelity of

$$p_{detect} = 93 \pm 5\%. \tag{6.6}$$

Also for this method we can get a more accurate estimation of the total photon number, by summing up the raw counts and dividing the outcome by the gain. The result is shown in the second histogram of Figure 6.10.

Another nice feature of this method is that it provides a good way to subtract the spurious-noise background from an image. For this, all clusters with a size below a threshold of 5 are removed from the image. Figure 6.11 shows this procedure applied

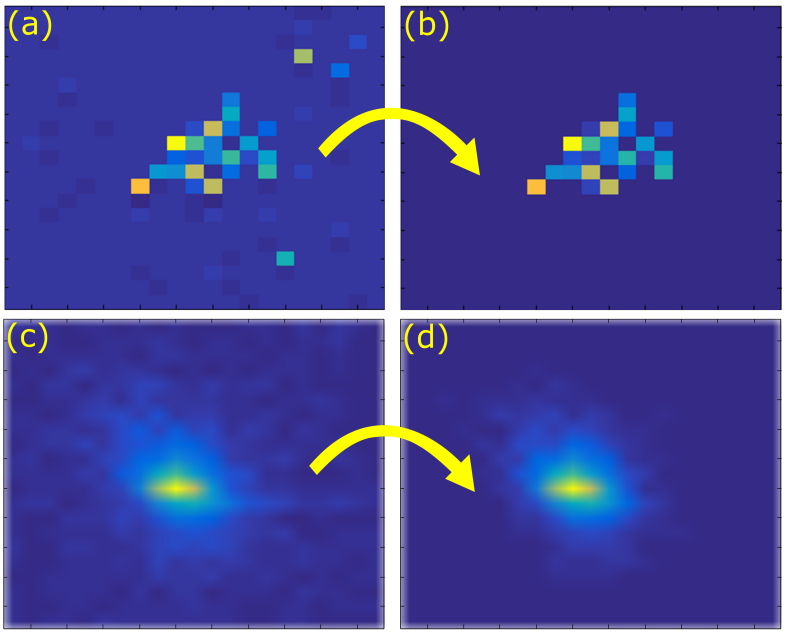

Figure 6.11: The cluster analysis provides a tool to remove the noisy background of an averaged image. For this all clusters with a size below the threshold are removed. Hence only the signal from the atoms is retained. Averaging the corrected images result in an image with a flat background since both the read noise and the spurious charges were removed.

to a single raw image. By averaging the corrected images, both the read noise of the background and the noise caused by spurious charges gets eliminated.

6.2 Counting atoms

Another aim of the imaging setup is the ability to count identical atoms on the same site. The detection of two distinguishable atoms on one site is reduced to identifying single atoms since the two different spin states are imaged on two separate pictures. However, if two indistinguishable atoms are occupying the same site, we need more photons such that the signal from one atom and from two atoms clearly separate.
If we detect n photons per atom on average, the distribution of detected photons is a Poisson distribution with mean n, $\mathscr{P}(n)$. Hence the signal of two atoms is a Poisson distribution with mean $2n$, $\mathscr{P}(2n)$. In order to clearly separate the signal of one and two atoms, the photon number per atom n must be so high, that $\mathscr{P}(n)$ and $\mathscr{P}(2n)$ separate. The first graph in Figure 6.12 shows plots of the function $\mathscr{P}(n) + \mathscr{P}(2n)$ for different n.
In this graph one can see that we need at least around $30 - 40$ photons per atom in order to clearly distinguish 2 atoms from 1. For an average number of 35 photons per

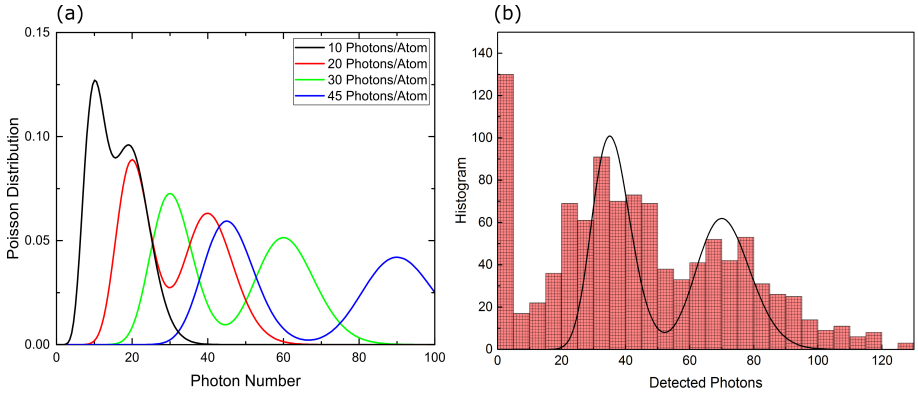

Figure 6.12: The left graph shows plots of the function $\mathscr{P}(n)+\mathscr{P}(2n)$ for different n. To distinguish 1 atom from 2 atoms, we need at least 30-40 photons per atom. The right graph shows the a histogram for a measurement where we prepared one and two atoms in a singe well and imaged over 23 μs. The measured distribution is broader than the plotted Poisson distribution with a mean of $\mu = 35$ due to a broadening by the stochastic amplification process within the gain register of the EMCCD-camera.

atom, the two Poisson distribution overlap by less than 1 %. Assuming a detection rate of 1.6 photons/μs as was measured in section 4.5, we need an imaging time of around 22 μs for this. As explained, such a long imaging time will later limit the site resolution in a multiwell potential due to the diffusion of the particle.

However, in order to count atoms in a single well, we prepared either one or two atoms in state $|3\rangle$ and imaged them for 23 μs. Since in this regime, we are dealing with relatively many photons, we determined the bright pixels with the cluster method. In order to also take multiple charges per pixel into account, the photon number is estimated by summing up the raw counts and dividing by the gain as was explained in the Section 6.1.1. Figure 6.12(b) shows a histogram of the experimental data and also a plot of the aforementioned function $\mathscr{P}(n) + \mathscr{P}(2n)$ with $n = 35$. In the experimental data one can clearly see a dip between the data of one and two atoms but the contrast is not very high. The data is also not well described by the Poisson plot but is much broader. The reason for this is that due to the stochastic amplification in the EM-mode, the estimation of the photon number with the described method has a certain width as was also analyzed in Chapter 4. Hence our estimation is the convolution of the Poisson (for the number of collected photons) and the transfer function of the gain register of the EMCCD camera. This broadens the outcome so that even higher photon numbers are required for counting two atoms on one well. As was analyzed in Chapter 4, state $|3\rangle$ has a completely closed optical transition so that we can further increase the photon number by imaging for longer times.

7 Conclusion and Outlook

This thesis reports on the implementation of a setup for fluorescence imaging with single atom resolution. Unlike other methods, we image the atom for only a few microseconds to collect few photons on a single-photon sensitive camera. This makes the pinning of atoms in a deep potential unnecessary. In the course of this thesis, we could demonstrate a detection fidelity of a single atom of $96 \pm 5\,\%$.

For the single atom detection, we illuminate the atom on the D_2 line with two counterpropagating imaging beams. We focus the fluorescence signal in the perpendicular direction with a high-resolution objective onto an EMCCD camera. By using horizontally polarized imaging light, which is perpendicular to the magnetic field, the atoms experience both σ_+ and σ_- polarized light. Due to the large splitting of the different fine structure states in the excited states, we can tune the frequency of our laser such that only the σ_- transition is the relevant imaging transition. It was analyzed and measured that we can almost close the optical transition of the two lowest hyperfine states $|1\rangle$ and $|2\rangle$ of the ground state by increasing the magnetic field to values over 900 G. State $|3\rangle$ features a completely closed optical transition.

Even though the number of collected photons is enhanced by the dipole radiation pattern as was shown in 4.3, the short imaging times only give rise to few photons on the camera. Within an imaging time of $11\,\mu$s we detect around 15 photons on the camera. For this we have to employ a CCD camera with EM-mode which was explained and analyzed in Chapter 5. A model for the output of the gain register was presented and used to determine the most relevant properties of the camera such as the gain and the read noise. It was shown that the most dominant noise source for EMCCD cameras are clock-induced charges, which can be influenced by adjusting the vertical shift speed of the camera. For the best settings we measured a probability of around $0.02\,\mathrm{e}^-/\mathrm{px}$. Other contributions to spurious noise can be neglected.
After we have gained a good understanding of the dipole transitions and the EM-mode of the camera, Chapter 6 applies this knowledge to identify single atoms.

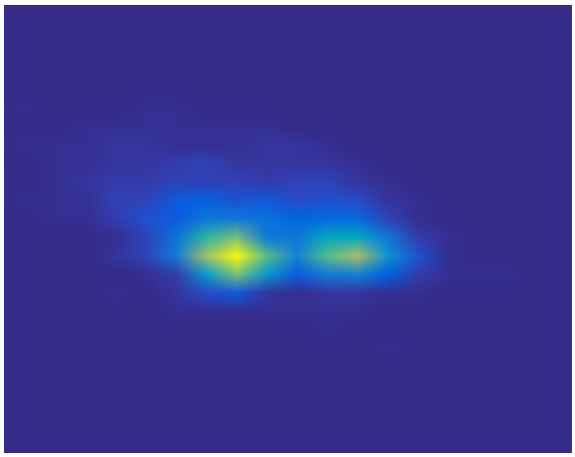

Figure 7.1: The image shows many atoms in a double-well potential. The two wells are separated by about 10 μm. Our next step is to prepare single atoms in this potential to realize a single atom, site-resolved imaging setup.

Different methods are developed and applied to the experimental data. With the different developed methods, we can identify single atoms with a fidelity of $96 \pm 5\,\%$. We were able to increase the detection fidelity by ramping the trapping potential to $27 E_{rec}$ before imaging. This countered the diffusion of the atom during the imaging process so that more signal could be accumulated within a smaller region of interest.

7.1 Outlook

Our simple method will allow us to detect atoms with spin and site resolution. For obtaining site-resolution, the diffusion length of the atom during the imaging process must be much smaller than the separation of two neighboring wells. We can already expand our system to a double-well potential with a separation of around 10 μm between the two wells. Figure 7.1 shows an image of many atoms in a such a potential, recorded with the new imaging technique. We will try to image single atoms in the potential very soon. For this we still need to understand the diffusion of the atom within the trapping potential.

Furthermore we will expand our setup to simultaneously image two spin states. For this we exploit that we can close the optical transition of each spin state by ramping the magnetic field to values over 900 G. In this regime, the hyperfine states of the ground state of ^{6}Li are separated by approximately 80 MHz so that we can address each spin state separately. For simultaneous imaging we will operate our camera in fast kinetics mode which allows us to take two images within a few microseconds. We record an image of one spin state, then we jump with the laser frequency [44]

by approximately 80 MHz to become resonant to the other spin state which we can image on a second imaging flash.
With these expansions to the imaging setup, we can reconstruct the full quantum state of the atomic system to study spin ordering and measure entanglement in a few-body system. Our imaging method will also be applicable to larger lattice systems when the lattice spacing can be increased to become larger than the diffusion length e.g. by using a spatial light modulator [45].

Bibliography

[1] Karl D Nelson, Xiao Li, and David S Weiss. Imaging single atoms in a three-dimensional array. *Nature Physics*, 3(8):556–560, 2007.

[2] Richard P Feynman. Simulating physics with computers. *International journal of theoretical physics*, 21(6):467–488, 1982.

[3] J Ignacio Cirac and Peter Zoller. Goals and opportunities in quantum simulation. *Nature Physics*, 8(4):264–266, 2012.

[4] Rudolf Grimm, Matthias Weidemüller, and Yurii B Ovchinnikov. Optical dipole traps for neutral atoms. *arXiv preprint physics/9902072*, 1999.

[5] Takeshi Fukuhara, Adrian Kantian, Manuel Endres, Marc Cheneau, Peter Schauß, Sebastian Hild, David Bellem, Ulrich Schollwöck, Thierry Giamarchi, Christian Gross, et al. Quantum dynamics of a mobile spin impurity. *Nature Physics*, 9(4):235–241, 2013.

[6] Leticia Tarruell, Daniel Greif, Thomas Uehlinger, Gregor Jotzu, and Tilman Esslinger. Creating, moving and merging dirac points with a fermi gas in a tunable honeycomb lattice. *Nature*, 483(7389):302–305, 2012.

[7] Alexander L Gaunt, Tobias F Schmidutz, Igor Gotlibovych, Robert P Smith, and Zoran Hadzibabic. Bose-einstein condensation of atoms in a uniform potential. *Physical Review Letters*, 110(20):200406, 2013.

[8] A Celi, P Massignan, J Ruseckas, N Goldman, IB Spielman, G Juzeliūnas, and M Lewenstein. Synthetic gauge fields in synthetic dimensions. *Physical review letters*, 112(4):043001, 2014.

[9] Simon Murmann, Frank Deuretzbacher, Gerhard Zürn, Johannes Bjerlin, Stephanie M Reimann, Luis Santos, Thomas Lompe, and Selim Jochim. Antiferromagnetic heisenberg spin chain of a few cold atoms in a one-dimensional trap. *Physical review letters*, 115(21):215301, 2015.

[10] Christof Weitenberg, Manuel Endres, Jacob F Sherson, Marc Cheneau, Peter Schauss, Takeshi Fukuhara, Immanuel Bloch, and Stefan Kuhr. Single-spin addressing in an atomic mott insulator. *Nature*, 471(7338):319–324, 2011.

[11] S Baier, MJ Mark, D Petter, K Aikawa, L Chomaz, Z Cai, M Baranov, P Zoller, and F Ferlaino. Extended bose-hubbard models with ultracold magnetic atoms. *arXiv preprint arXiv:1507.03500*, 2015.

[12] Lijun Yang, Xiwen Guan, and Xiaoling Cui. Engineering quantum magnetism in one-dimensional trapped fermi gases with p-wave interactions. *arXiv preprint arXiv:1511.09377*, 2015.

[13] F Deuretzbacher, D Becker, Johannes Bjerlin, SM Reimann, and L Santos. Quantum magnetism without lattices in strongly interacting one-dimensional spinor gases. *Physical Review A*, 90(1):013611, 2014.

[14] Jonathan Simon, Waseem S Bakr, Ruichao Ma, M Eric Tai, Philipp M Preiss, and Markus Greiner. Quantum simulation of antiferromagnetic spin chains in an optical lattice. *Nature*, 472(7343):307–312, 2011.

[15] Monika Aidelsburger, Marcos Atala, Sylvain Nascimbène, Stefan Trotzky, Y-A Chen, and Immanuel Bloch. Experimental realization of strong effective magnetic fields in an optical lattice. *Physical review letters*, 107(25):255301, 2011.

[16] W Ketterle, DS Durfee, and DM Stamper-Kurn. Making, probing and understanding bose-einstein condensates. *arXiv preprint cond-mat/9904034*, 5, 1999.

[17] PA Murthy, D Kedar, T Lompe, M Neidig, MG Ries, AN Wenz, G Zürn, and S Jochim. Matter-wave fourier optics with a strongly interacting two-dimensional fermi gas. *Physical Review A*, 90(4):043611, 2014.

[18] M. Greiner, C. A. Regal, J. T. Stewart, and D. S. Jin. Probing pair-correlated fermionic atoms through correlations in atom shot noise. *Phys. Rev. Lett.*, 94:110401, Mar 2005.

[19] Waseem S Bakr, Jonathon I Gillen, Amy Peng, Simon Fölling, and Markus Greiner. A quantum gas microscope for detecting single atoms in a hubbard-regime optical lattice. *Nature*, 462(7269):74–77, 2009.

[20] Lawrence W Cheuk, Matthew A Nichols, Melih Okan, Thomas Gersdorf, Vinay V Ramasesh, Waseem S Bakr, Thomas Lompe, and Martin W Zwierlein. Quantum-gas microscope for fermionic atoms. *Physical review letters*, 114(19):193001, 2015.

[21] Martin Miranda, Ryotaro Inoue, Yuki Okuyama, Akimasa Nakamoto, and Mikio Kozuma. Site-resolved imaging of ytterbium atoms in a two-dimensional optical lattice. *Physical Review A*, 91(6):063414, 2015.

[22] Christian Groß. Atomic physics: Fermions under the microscope. *Nature Photonics*, 9(8):482–483, 2015.

[23] Maxwell F Parsons, Florian Huber, Anton Mazurenko, Christie S Chiu, Widagdo Setiawan, Katherine Wooley-Brown, Sebastian Blatt, and Markus Greiner. Site-resolved imaging of fermionic li 6 in an optical lattice. *Physical review letters*, 114(21):213002, 2015.

[24] Waseem S Bakr, Amy Peng, M Eric Tai, Ruichao Ma, Jonathan Simon, Jonathon I Gillen, Simon Foelling, Lode Pollet, and Markus Greiner. Probing the superfluid–to–mott insulator transition at the single-atom level. *Science*, 329(5991):547–550, 2010.

[25] Philipp M Preiss, Ruichao Ma, M Eric Tai, Jonathan Simon, and Markus Greiner. Quantum gas microscopy with spin, atom-number, and multilayer readout. *Physical Review A*, 91(4):041602, 2015.

[26] Ahmed Omran, Martin Boll, Timon A Hilker, Katharina Kleinlein, Guillaume Salomon, Immanuel Bloch, and Christian Gross. Microscopic observation of pauli blocking in degenerate fermionic lattice gases. *Physical review letters*, 115(26):263001, 2015.

[27] Simon Murmann, Andrea Bergschneider, Vincent M Klinkhamer, Gerhard Zürn, Thomas Lompe, and Selim Jochim. Two fermions in a double well: Exploring a fundamental building block of the hubbard model. *Physical review letters*, 114(8):080402, 2015.

[28] DB Hume, I Stroescu, M Joos, W Muessel, H Strobel, and MK Oberthaler. Accurate atom counting in mesoscopic ensembles. *Physical review letters*, 111(25):253001, 2013.

[29] Jacob F Sherson, Christof Weitenberg, Manuel Endres, Marc Cheneau, Immanuel Bloch, and Stefan Kuhr. Single-atom-resolved fluorescence imaging of an atomic mott insulator. *Nature*, 467(7311):68–72, 2010.

[30] Steffen Wolf, Steven J Oliver, and David S Weiss. Suppression of recoil heating by an optical lattice. *Physical review letters*, 85(20):4249, 2000.

[31] Michael E Gehm. Properties of 6li. *Jetlab,*, 2003.

[32] Jonathan Förste. The ac-stark shift of lithium-6 in a dipole trap, 2015. Bachelor's thesis, Ruprecht-Karls-Universität Heidelberg.

[33] Simon Murmann. Few-particle quantum magnetism with ultracold atoms, 2015. PhD thesis, Ruprecht-Karls-Universität Heidelberg.

[34] Friedhelm Serwane. The setup of a magneto optical trap for the preparation of a mesoscopic degenerate fermi gas, 2007. Diploma thesis, Ruprecht-Karls-Universität Heidelberg.

[35] Gerhard Zürn. Few-fermion systems in one dimension. 2012. PhD thesis, Ruprecht-Karls-Universität Heidelberg.

[36] Andrea Bergschneider. Ultracold few-fermion systems in multiwell potentials, 2013. Master thesis, Ruprecht-Karls-Universität Heidelberg.

[37] Martin Ries. A magneto-optical trap for the preparation of a three-component fermi gas in an optical lattice, 2010. Diploma thesis, Ruprecht-Karls-Universität Heidelberg.

[38] David DeMille Dmitry Budker, Derek F. Kimball. *Atomic physics: an exploration through problems and solutions*. Oxford Univ. Press, 2010.

[39] Andor Technology. Emccds for spectroscopy. http://www.andor.com/learning-academy/emccds-for-spectroscopy-emccd-technology-in-spectroscopy. 23.03.2016.

[40] Michael Hirsch, Richard J Wareham, Marisa L Martin-Fernandez, Michael P Hobson, and Daniel J Rolfe. A stochastic model for electron multiplication charge-coupled devices–from theory to practice. *PloS one*, 8(1):e53671, 2013.

[41] Olivier et al Daigle. Cccp: a ccd controller for counting photons. In *SPIE Astronomical Telescopes+ Instrumentation*, pages 70146L–70146L. International Society for Optics and Photonics, 2008.

[42] AG Basden, CA Haniff, and CD Mackay. Photon counting strategies with low-light-level ccds. *Monthly notices of the royal astronomical society*, 345(3):985–991, 2003.

[43] Marc AN Korevaar, Marlies C Goorden, Jan WT Heemskerk, and Freek J Beekman. Maximum-likelihood scintillation detection for em-ccd based gamma cameras. *Physics in medicine and biology*, 56(15):4785, 2011.

[44] Thomas Steinle. Implementation of simultaneously imaging two hyperfine states of ultracold 6li atoms in a magnetic field, 2015. Bachelor's thesis, Ruprecht-Karls-Universität Heidelberg.

[45] Marvin Holten. Hamiltonian engineering in ultracold atom experiments using a spatial light modulator, 2014. Bachelor's thesis, Ruprecht-Karls-Universität Heidelberg.

8 Danksagung

Ich möchte mich bei allen bedanken, die mir beim Entstehen dieser Arbeit geholfen haben und mich im Laufe meines Studiums unterstützt haben.
Ein ganz besonderer Dank gilt der gesamten Arbeitsgruppe. Vor allem danke ich Selim für die gute Betreuung, viele interessante Diskussionen und dafür, dass er mich motivieren konnte, als bei mir die Motivation knapp war.
Besonderer Dank gilt Andrea für die viele Geduld und die Hilfe in der entscheidenden Phase dieser Arbeit und auch für viele tolle Stunden im Labor. Ohne dich wäre diese Arbeit so vermutlich nicht möglich gewesen.
Ich danke Mathias, Vincent, Puneet, Luca, Michael, Ralf, Thomas und Peter für die lustige Zeit im Büro, im Labor und beim Kickern und Kuchenessen in der CQD-Lounge.
Vielen Dank an Herrn JProf. Dr. Fred Jendrzejewski für die Übernahme der Zweitkorrektur dieser Arbeit.
Ein ganz besonderer Dank meiner Familie und meinen Freunden, die mich in den letzten 5 Jahren in meinem Studium begleitet und mir eine unvergessliche Zeit in Heidelberg bereitet haben. Danke!

Erklärung

Ich versichere, dass ich diese Arbeit selbstständig verfasst und keine anderen als die angegebenen Quellen und Hilfsmittel benutzt habe.

Heidelberg, den 01.04.2016

.....

(Unterschrift) Unterschrift